Chemical Geology 679 (2025) 122671

Contents lists available at ScienceDirect

Chemical Geology

journal homepage: www.elsevier.com/locate/chemgeo

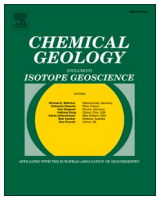

Chalcophile and siderophile element (CSE) partitioning between sulfide liquid and silicate melt and the role of the "Hadean matte"

Mingdong Zhang [a], Yuan Li [b,*]

[a] School of Earth Science, Yunnan University, Kunming 650500, China
[b] Bayerisches Geoinstitut, Universität Bayreuth, 95440 Bayreuth, Germany

ARTICLE INFO

Editor: Claudia Romano

Keywords:
Chalcophile and siderophile elements
Sulfide liquids
Partition coefficients
Hadean matte
Earth's magma ocean

ABSTRACT

This study evaluates the role of mantle-to-core segregation of the "Hadean matte" (sulfide liquids) occurring in the solidifying magma ocean in determining the chalcophile and siderophile element (CSE) abundances of the silicate Earth. The partition coefficients of CSEs between sulfide liquid and basaltic to peridotitic melt ($D_{CSE}^{Sul/Sil}$) were determined at 1–14 GPa and 1300–2100 °C. The variations in the obtained $D_{CSE}^{Sul/Sil}$ (30–160 for Co, 50–1200 for Ni, 40–940 for Cu, 20–210 for Mo, 50–210 for Ag, 20–90 for Cd, 4–60 for In, 30–150 for Sb, 3900–30,000 for Re, 15–210 for Pb, 140–1700 for Bi, 0.3–7 for Zn, 0.7–7 for Ge, and 0.1–0.9 for Ga) can be explained and parameterized as a function of the experimental pressure, temperature, and composition of the silicate melt and sulfide liquid. Application of the $D_{CSE}^{Sul/Sil}$ parameterization to the mantle-to-core segregation of sulfide liquids in a deep magma ocean at 75 GPa shows that less than 10 % of each of Co, Ni, Cu, Zn, Ga, Ge, Mo, Ag, Cd, In, Sb, Pb, and Bi in the silicate Earth can be sequestered in the core; whereas, in a shallow magma ocean at 10 GPa, 50–80 % of each of Cu, Ag, and Bi and less than 50 % of the other CSEs can be sequestered in the core. In contrast, mantle-to-core segregation of sulfide liquids could have extracted more than 90 % of the Re in the silicate Earth in both cases, requiring the addition of a late veneer to explain the present-day mantle value. Our results demonstrate that if Earth's volatile CSEs (Cu, Zn, Ga, Ge, Ag, Cd, In, Sb, Pb, and Bi) were delivered when metal segregation to the core was largely inactive, the depletion pattern of volatile CSEs relative to the lithophile elements of similar volatility in the silicate Earth cannot be explained by mantle-to-core segregation of sulfide liquids. Also, previous models that used mantle-to-core segregation of sulfide liquids as an important approach to explain the depletion of volatile CSEs in the silicate Earth need to be re-examined.

1. Introduction

As a major host of chalcophile and siderophile elements (CSEs), sulfide liquids are commonly present in magmas associated with the large-scale differentiation of the Earth's core, mantle, and crust. During the differentiation of the Earth's crust and mantle, sulfide liquids are present in both mid-ocean ridge basalts and oxidized arc magmas, exerting a strong control on the transfer of CSEs from the mantle (Bockrath et al., 2004; Chang and Audétat, 2018; Jenner, 2017; Jenner et al., 2010; Kiseeva et al., 2017; Lee et al., 2012; Li et al., 2021; Liu and Li, 2023; Mungall and Brenan, 2014; Zhang and Li, 2021). During the differentiation of the Earth's mantle and core, the delivery of volatiles during the Earth's late accretion stages may have resulted in the saturation of sulfide liquids in the proto-mantle, termed the "Hadean matte" (O'Neill, 1991). They may have subsequently segregated into the core, significantly affecting the abundances of CSEs in the silicate Earth (Ballhaus et al., 2017; Ballhaus et al., 2013; Kiseeva and Wood, 2015; Laurenz et al., 2016; Righter et al., 2018; Righter et al., 2020; Rubie et al., 2016; Wood et al., 2008; Wood et al., 2006). The sulfide liquid–silicate melt partition coefficients of CSEs ($D_{CSE}^{Sul/Sil}$) represent a crucial parameter for quantifying the distribution of CSEs between the mantle and crust, and between the core and mantle given the mantle-to-core segregation of sulfide liquids. In combination with the observed present-day CSE abundances of the silicate Earth, this parameter can be further employed to constrain the Earth's accretion process and the delivery of essential volatile elements for life (Ballhaus et al., 2017; Ballhaus et al., 2013; Laurenz et al., 2016; Righter et al., 2018; Righter et al., 2020; Rubie et al., 2016). For example, to explain the relative-

* Corresponding author.
E-mail address: Yuan.Li@uni-bayreuth.de (Y. Li).

https://doi.org/10.1016/j.chemgeo.2025.122671
Received 17 October 2024; Received in revised form 29 January 2025; Accepted 1 February 2025
Available online 10 February 2025

chondritic platinum-group-element (PGE) abundances of the silicate Earth, mantle-to-core segregation of sulfide liquids, with sulfide liquid–silicate melt partition coefficients of PGEs ($D_{PGE}^{Sul/Sil}$) > 10^5, must have occurred in the Earth's deep magma ocean prior to the addition of a chondritic late veneer (Laurenz et al., 2016; Righter et al., 2018; Rubie et al., 2016). Such a chondritic late veneer may have not only delivered PGEs (Dale et al., 2012; Day et al., 2016), but also contributed water, carbon, and nitrogen to the proto-Earth (Albarede, 2009; Marty, 2012; Varas-Reus et al., 2019; Wang and Becker, 2013), although the precise role of the late veneer in the origin of the Earth's volatiles remains a topic of contention (Broadley et al., 2022; Labidi et al., 2013; Marty, 2012; Shi et al., 2022; Wang et al., 2021).

In order to gain insights into the role played by sulfide liquids in the distribution of CSEs between the mantle and the crust, experimental determinations of $D_{CSE}^{Sul/Sil}$ for V, Cr, Mn, Co, Ni, Cu, Zn, Ga, Ge, As, Se, Mo, Ag, Cd, Sn, Sb, Te, W, Re, Au, Tl, Pb, and Bi have been made primarily at the Earth's crust–mantle pressure (P) and temperature (T) conditions ($P \leq 3$ GPa and $T \leq 1700$ °C), which are more pertinent to the processes of mantle partial melting and subsequent magmatic differentiation (Botcharnikov et al., 2013; Brenan, 2008; Brenan, 2015; Brenan et al., 2015; Feng and Li, 2019; Gaetani and Grove, 1997; Kiseeva and Wood, 2013; Kiseeva and Wood, 2015; Li, 2014; Li and Audétat, 2012; Li and Audétat, 2015; Li et al., 2021; Li et al., 2019; Mungall and Brenan, 2014; Peach and Mathez, 1993). The principal findings of these preceding studies are that $D_{CSE}^{Sul/Sil}$ vary within the range of 10–10^6 and are a robust function of temperature, the composition of silicate melt and sulfide liquid, and oxygen fugacity (fO_2) for the elements with multiple valence states. The $D_{CSE}^{Sul/Sil}$ are typically observed to increase with decreasing FeO_{tot} content of the silicate melt and temperature, although the silicate melt composition varied from basaltic to rhyolitic; however, there are exceptions, with some elements, such as Ge and Ga, exhibiting an increase in $D_{CSE}^{Sul/Sil}$ with temperature (Kiseeva and Wood, 2013; Kiseeva and Wood, 2015; Li and Audétat, 2015; Li et al., 2021). In the case of the CSEs with multiple valence states, such as Re, Mo, and Sn, the $D_{CSE}^{Sul/Sil}$ have been observed to increase with a decrease in fO_2 (Brenan, 2008; Feng and Li, 2019; Li and Audétat, 2015; Li et al., 2021). The experimental determinations of $D_{CSE}^{Sul/Sil}$ for PGEs by using the coexisting sulfide liquid and silicate melt and the in-situ micro-analytical method of LA–ICP–MS have yielded results that are not entirely consistent with one another, but which nonetheless offer some intriguing results (Mungall and Brenan, 2014; Wang and Li, 2024; Zhang and Li, 2021). Mungall and Brenan (2014) obtained $D_{PGE}^{Sul/Sil}$ values greater than 10^5 at 1 bar and 1200 °C. However, the results of Zhang and Li (2021) demonstrated that the $D_{Pt,Pd}^{Sul/Sil}$ values (ranging from 10^3 to 10^5) increase with the addition of Pt and Pd to the sulfide liquids at 1 GPa and 1400 °C and fO_2 below the fayalite–magnetite–quartz (FMQ) buffer. Nevertheless, such concentration-dependence of $D_{Pt,Pd}^{Sul/Sil}$ was not observed at 1.5 GPa and 1400 °C and at fO_2 1.5–2 log units above the FMQ buffer (Wang and Li, 2024). The concentration-dependance of $D_{Pt,Pd}^{Sul/Sil}$ was explained by using the non-Henrian law and the formation of Pt- and/or Pd-rich nuggets in the sulfide liquids at fO_2 below the FMQ buffer (Ballhaus and Sylvester, 2000; Liu and Li, 2023; Wang and Li, 2024; Zhang and Li, 2021).

Mantle-to-core segregation of sulfide liquids may have occurred in the Earth's deep magma ocean at pressures >30 GPa and temperatures >2500 °C (Blanchard et al., 2021; Laurenz et al., 2016; Righter et al., 2018; Righter et al., 2020; Rubie et al., 2016). However, only Laurenz et al. (2016) have thus far measured $D_{CSE}^{Sul/Sil}$ for Pt, Pd, Ru, and Ir at P–T conditions (7–21 GPa and 2100–2400 °C) that are more relevant for the Earth's deep magma ocean. Using the available $D_{PGE}^{Sul/Sil}$ (Laurenz et al., 2016; Mungall and Brenan, 2014), previous authors have shown that the quantitative interpretation of the relative-chondritic PGE abundances of the silicate Earth is highly dependent on the mantle-to-core segregation of sulfide liquids occurring in the Earth's deep magma ocean (Laurenz et al., 2016; Righter et al., 2018; Rubie et al., 2016). Mantle-to-core segregation of sulfide liquids has also been proposed to explain the depletion of volatile CSEs (e.g., Cu, Ag, Bi, As, Se, and Te) in the silicate Earth relative to the lithophile elements of similar volatility (e.g., Li, Na, K, Rb, and F) (Ballhaus et al., 2017; Ballhaus et al., 2013; Kiseeva and Wood, 2015; O'Neill, 1991; Righter et al., 2018; Yoshizaki and McDonough, 2021), as well as the isotopic systematics of Cu, Pd-Ag, and U-Pb in the silicate Earth (Ballhaus et al., 2013; Hart and Gaetani, 2006; Righter et al., 2020; Savage et al., 2015; Wood et al., 2008). In particular, it has been suggested that if the Earth's volatiles were delivered late, when metal segregation to the core was largely inactive, the large depletion of sulfur and volatile CSEs in the silicate Earth may have to be attributed to the core-to-mantle segregation of sulfide liquids occurring in an oxidized and largely crystalline mantle (Ballhaus et al., 2017; Kiseeva and Wood, 2015; O'Neill, 1991). However, we note that due to the lack of relevant experimental $D_{CSE}^{Sul/Sil}$ for volatile CSEs, previous authors had to use the $D_{CSE}^{Sul/Sil}$ obtained at crust–mantle conditions to assess the role of sulfide liquids in determining the volatile CSE abundances and isotopic compositions of the silicate Earth. Indeed, even pressure and/or temperature have small effects on $D_{CSE}^{Sul/Sil}$, which may be sufficient to cause the corresponding $D_{CSE}^{Sul/Sil}$ values for the magma ocean to differ significantly from the $D_{CSE}^{Sul/Sil}$ values obtained at crust–mantle conditions. Consequently, this could lead to a very different understanding of the role that mantle-to-core segregation of sulfide liquids had in determining the volatile CSE abundances and isotopic compositions of the silicate Earth. In addition, none of previous studies has determined $D_{CSE}^{Sul/Sil}$ in the sulfide liquid–peridotitic melt systems, where the mantle-to-core segregation of sulfide liquids could have happened, and it remains unknown whether high MgO contents of the silicate melts could influence $D_{CSE}^{Sul/Sil}$.

In this study, we present new laboratory experiments that aimed at determining $D_{CSE}^{Sul/Sil}$ for Co, Ni, Cu, Zn, Ga, Ge, Mo, Ag, Cd, In, Sb, Re, Pb, and Bi in the sulfide liquid–basaltic to peridotitic melt systems at pressures of 1–14 GPa and temperatures of 1300–2100 °C. Combined with previous partitioning data obtained at crust–mantle conditions as described above, and following previous partitioning models (Kiseeva and Wood, 2013; Kiseeva and Wood, 2015; Li and Audétat, 2015; Li et al., 2021), our new $D_{CSE}^{Sul/Sil}$ are parameterized as a multifunction of P–T and composition of the silicate melt and sulfide liquid. We then use this parameterization to quantify the effect that mantle-to-core segregation of sulfide liquids could have on the CSE abundances of the silicate Earth.

2. Methods

2.1. Starting materials

Starting materials included synthetic silicates and sulfides. The synthetic silicates had major element compositions similar to those of average mid-ocean ridge basalt (MORB), the Earth's mantle pyrolite (McDonough and Sun, 1995), and Martian olivine-phyric basaltic shergottite (Y98) (Shirai and Ebihara, 2004). The use of these different silicates facilitates the investigation of the effect of silicate melt composition on $D_{CSE}^{Sul/Sil}$. The starting silicates were prepared from analytical grade oxides and carbonates. To minimize the amount of water absorbed, the SiO_2, TiO_2, Al_2O_3, Cr_2O_3, and MgO powders were each heated overnight at 1000 °C, MnO_2 at 400 °C, $CaCO_3$ at 200 °C, and Na_2CO_3 and K_2CO_3 at 110 °C. All dried oxides and carbonates were mixed and ground in acetone in a mortar and then dried overnight at room temperature. Well mixed oxide and carbonate powder was sintered in a high purity alumina crucible at 1000 °C overnight to decarbonate. The decarbonated powder was finally mixed with FeO powder and ground in acetone in a mortar and dried at room temperature.

The sulfides were prepared from mixtures of analytical grade FeS, Cu_2S, NiS, and metallic powders of trace elements. The sulfides contain ~0.5–7 wt% Cu and Ni and trace amounts of Co, Zn, Ga, Ge, Mo, Ag, Cd, In, Sb, Re, Pb, and Bi (< 5000 μg/g in total). The weighed FeS, Cu_2S, NiS, and trace element powders were mixed and ground in ethanol in an agate mortar for 1 h and then dried at room temperature. Prior to use, all the dried powder mixtures were stored in a drying oven at 100 °C to prevent the introduction of moisture from the air. The major and trace element compositions of the starting silicates and sulfides are given in Table 1.

2.2. High-pressure experiments

Thirty-six high-pressure experiments were conducted to determine $D_{CSE}^{Sul/Sil}$ as a function of pressure, temperature, and composition of the silicate melt and the sulfide liquid. Mixtures of ~60–70 wt% silicate and ~ 30–40 wt% sulfide were loaded into graphite capsules or single crystal MgO capsules. Twenty-five experiments were conducted at 1–3 GPa and 1300–1800 °C in an end-loaded, solid media piston-cylinder apparatus (Max Voggenreiter LPC250), using 1/2-in. diameter talc-pyrex assemblies with graphite heaters. The pressure was calibrated against the quartz–coesite (Bose and Ganguly, 1995) and kyanite–sillimanite (Bohlen et al., 1991) transitions and a friction correction of 20 % was applied to the nominal pressure. The total pressure uncertainty was less than 0.1 GPa. The temperature of the experiments was monitored using $W_{95}Re_{05}$–$W_{74}Re_{26}$ (type C) thermocouples with an estimated temperature uncertainty of ±10 °C. Eleven experiments were conducted at 4–14 GPa and 2000–2100 °C in a 2500-ton multi-anvil apparatus. The pressure media consisted of Cr_2O_3-doped MgO octahedra with 14 mm edges. Cubic tungsten carbide anvils with 8 mm truncations (14/8 configurations) were used to apply pressure to the sample along three primary axes. Experimental pressures were estimated from the hydraulic pressure using calibrations based on the phase transitions of Bi (I-II) and ZnS at room temperature, and based on the SiO_2 (coesite–stishovite) and $MgSiO_3$ (ilmenite–perovskite) phase transitions at 1600 °C (Liu et al., 2018). A stepped $LaCrO_3$ heater was used to minimize temperature gradients. The octahedron, MgO spacer, and $LaCrO_3$ heater were dried at 1000 °C for 10 h prior to each experiment. The temperatures of the experiments were monitored using $W_{95}Re_{05}$–$W_{74}Re_{26}$ (type C) thermocouples. The temperature fluctuation during the experiments was approximately ±10 °C.

All experiments were first pressurized at room temperature and then heated at a rate of 50 °C/min. To reduce the porosity of the graphite capsules and thus prevent the leakage of sulfide liquids, the experiments were first heated to 850 °C and held for 2–4 h before being raised to the target temperatures. All experiments were quenched by switching off the electrical power to the heaters. The experimental durations ranged from 15 min to 48 h, depending on the experimental temperatures. Many previous studies have shown that these experimental durations are long enough to reach equilibrium partitioning of CSEs between sulfide liquid and silicate melt in capsules of similar size (Feng and Li, 2019; Kiseeva and Wood, 2013; Kiseeva and Wood, 2015; Li and Audétat, 2012; Li and Audétat, 2015; Li et al., 2021). The recovered samples were mounted in resin and polished for scanning electron microscopy (SEM) observations, electron probe microanalysis (EPMA), and laser ablation–inductively coupled plasma–mass spectroscopy (LA–ICP–MS) analyses.

2.3. Analytical methods

2.3.1. EPMA

The major element compositions of the quenched sulfide liquids and silicate melts were measured using a JEOL JXA-8530F Plus Field Emission EPMA. Beam sizes of 10 and 30 μm were used for the analyses of the quenched silicate melts and sulfide liquids, respectively. The acceleration voltage was 15 kV at a current of 10 nA for all elements in the quenched silicate melts. The peak counting time was 20 s, except for Na and K, which were measured for 10 s. Natural and synthetic standards were used to calibrate the instrument; the used standards were diopside for Si, Mg and Ca, albite for Na, orthoclase for K, apatite for P, almandine garnet for Al, magnetite for Fe, Cr_2O_3 for Cr, rutile for Ti, $MnTiO_3$ for Mn, and pure metals for Cu and Ni. An acceleration voltage of 15 kV, a beam current of 70 nA, and a beam size of 20 μm were used to measure S in the quenched silicate melts. Pyrrhotite was used as the standard, and the peak counting time was 60 s. The quenched sulfide liquids were analyzed with 20 kV acceleration voltage and 20 nA beam current. Fe and S were calibrated against a synthetic pyrrhotite with a known Fe: S ratio, Ni and Cu against pure metals and O against magnetite.

2.3.2. LA–ICP–MS

The major and trace elements of the quenched silicate melts and sulfide liquids were measured using LA–ICP–MS. These analyses were carried out on an Agilent 7900 quadrupole ICP–MS coupled to a Photon Machines Analyte HE 193-nm ArF excimer laser ablation system. The

Table 1
Compositions of the starting silicates (in wt%) and sulfides (in wt% and μg/g).

	SiO_2	TiO_2	Al_2O_3	Cr_2O_3	FeO	MnO	MgO	CaO	Na_2O	K_2O	P_2O_5	Total
MORB	50.50	0.93	15.90	0.20	9.06	0.23	8.63	11.20	3.01	0.10	0.10	99.86
Pyrolite	45.10	0.20	4.45	0.20	7.60	0.13	37.80	3.50	0.35	0.03	0.02	99.38
Y98 Silicate	49.40	0.48	6.00	0.10	17.53	0.52	19.64	6.37	0.48	0.02	0.29	100.20

	Fe (wt %)	S (wt %)	Cu (wt %)	Ni (wt %)	Co (μg/g)	Zn (μg/g)	Ga (μg/g)	Ge (μg/g)	Mo (μg/g)	Ag (μg/g)	Cd (μg/g)	In (μg/g)	Sb (μg/g)	Re (μg/g)	Pb (μg/g)	Bi (μg/g)
Sulfide 01	54	36	7	3	30				700					800		
Sulfide 02	62	36	0.5	0.4	800				700	1000		3000		500		2000
Sulfide 03	58	34	2	5	700	1000							400			700
Sulfide 04	64	36			30	200	50	300			400	700	1000		1000	1500
Sulfide 05	64	36			30	200	50	300			400	700	1000		1000	1500
Sulfide 06	57	34	3	5			50	30	5000	1500	400	400	700	2000	100	1500

quenched silicate melts were analyzed with 10 Hz, 80 mJ, and laser beam sizes of 60–90 μm, while the quenched sulfide liquids were analyzed with 7 Hz, 70 mJ, and laser beam sizes of 30–50 μm. A typical time-resolved analysis included ~20 s of background acquisition followed by laser ablation for 40 s. Helium was used as carrier gas (0.9 L/min) and nitrogen gas was used as make-up gas (0.85 L/min), mixed with the carrier gas via a T-connector before entering the ICP. The isotopes ^{23}Na, ^{24}Mg, ^{27}Al, ^{29}Si, ^{32}P, ^{39}K, ^{42}Ca, ^{49}Ti, ^{52}Cr, ^{55}Mn, ^{57}Fe, ^{59}Co, ^{62}Ni, ^{65}Cu, ^{66}Zn, ^{71}Ga, ^{74}Ge, ^{98}Mo,^{107}Ag, ^{111}Cd, ^{115}In, ^{121}Sb, ^{208}Pb, and ^{209}Bi were measured with a dwell time of 10 ms. The detection limits were ~ 0.2–0.3 μg/g for Pb, 0.03–0.06 μg/g for Co, 0.11–0.21 μg/g for Cu, 0.36–0.44 μg/g for Ni, 0.43–0.51 μg/g for Zn, 0.06–0.08 μg/g for Mo, 0.013–0.016 μg/g for Ag, 0.04–0.06 μg/g for Sb, 0.01–0.02 μg/g for Bi, 0.007–0.01 μg/g for In, 0.40–0.70 μg/g for Ge, 0.03–0.05 μg/g for Ga, and 0.02–0.05 μg/g for Cd. To accurately measure ^{185}Re in the silicate melts, ^{185}Re was measured with a dwell time of 50 ms and the detection limits of Re were ~ 1–3 ng/g. NIST SRM 610 glass was used as an external standard for all analyses, while Si and Fe determined by EPMA were used as internal standards for the quenched silicate melts and sulfide liquids, respectively. The Mass-1 sulfide standard was used as an unknown sample to check the accuracy of the LA–ICP–MS analyses of the sulfide liquids. Repeated analyses of the Mass-1 sulfide standard after analysis of each ten spots yielded CSE concentrations that agreed with the certified values within 5–16 % relative. The overall uncertainties resulting from the internal and external standardization procedures are estimated to be better than 15–20 % for all elements 2–3 times above the detection limit (Li and Audétat, 2012; Li et al., 2021). LA–ICP–MS signal data were converted to concentration data using the program of Liu et al. (2008).

3. Results

3.1. Sample texture

An overview of the experimental *P–T* conditions, starting materials, sample capsules, run durations, and run products is given in Table 2. Representative sample textures are shown in Fig. 1. All experiments produced coexisting sulfide liquid and silicate melt. The silicate melts with a MORB-like composition were quenched to glasses in the experiments conducted at 1–6 GPa (Fig. 1a). In the other experiments, the quenched silicate melts show a dendritic texture (Fig. 1d), which is typical of the quenching of peridotitic melts and the quenching of basaltic melts from high-pressure multi-anvil experiments. Ferropericlase was observed in the two experiments using MgO capsule. In all experiments, minute sulfide dots are homogeneously distributed in the silicate melts (Fig. 1b), which were exsolved during quenching due to the decrease in sulfide solubility. Furthermore, during the quenching, the sulfide liquids exsolved into a fine-grained Fe-rich monosulfide-solid-solution and a Cu-rich sulfide phase (Fig. 1c), which has been observed in many previous studies on the sulfide liquid–silicate melt partitioning of CSEs (Ballhaus et al., 2006; Bockrath et al., 2004; Brenan, 2015; Feng and Li, 2019; Li and Audétat, 2012; Li and Audétat, 2013).

3.2. Major and trace element compositions of the silicate melts

The major and trace element compositions of the quenched silicate melts are given in Tables 3 and 4 and plotted in Fig. 2. The silicate melts of the experiments starting with MORB contain 48.2–51.2 wt% SiO_2, 13.7–17.7 wt% Al_2O_3, 7.5–10.2 wt% MgO, 6.4–9.5 wt% FeO_{tot}, and 10.1–12.4 wt% CaO. The silicate melts of the experiments starting with peridotite contain 42.1–46.3 wt% SiO_2, 4.7–6.8 wt% Al_2O_3, 32.7–38.3

Table 2
Summary of the experimental conditions and products.

Run. No	Pressure (GPa)	Temperature (°C)	Run duration	Starting composition	Capsule	Run products
ZD01	1	1300	48 h	MORB + Sulfide 01	Graphite	Sulfide liquid + Silicate melt
ZD02	1	1400	24 h	MORB + Sulfide 01	Graphite	Sulfide liquid + Silicate melt
ZD03	1	1500	10 h	MORB + Sulfide 01	Graphite	Sulfide liquid + Silicate melt
ZD04	1	1600	3 h	MORB + Sulfide 01	Graphite	Sulfide liquid + Silicate melt
ZD05	1	1700	2 h	MORB + Sulfide 01	Graphite	Sulfide liquid + Silicate melt
ZD07	3	1600	3 h	MORB + Sulfide 01	Graphite	Sulfide liquid + Silicate melt
ZD08	1	1800	30 min	MORB + Sulfide 01	Graphite	Sulfide liquid + Silicate melt
ZD13	8	2100	15 min	MORB + Sulfide 01	Graphite	Sulfide liquid + Silicate melt
ZD15	3	1800	30 min	MORB + Sulfide 01	Graphite	Sulfide liquid + Silicate melt
ZD16	4	2100	15 min	MORB + Sulfide 02	Graphite	Sulfide liquid + Silicate melt
ZD17	7	2100	15 min	MORB + Sulfide 02	Graphite	Sulfide liquid + Silicate melt
D01	1	1600	3 h	MORB + Sulfide 03	Graphite	Sulfide liquid + Silicate melt
D02	1	1700	2 h	MORB + Sulfide 03	Graphite	Sulfide liquid + Silicate melt
D03	1	1800	30 min	MORB + Sulfide 03	Graphite	Sulfide liquid + Silicate melt
BM1–13	1	1300	48 h	MORB + Sulfide 04	Graphite	Sulfide liquid + Silicate melt
BM1–14	1	1400	24 h	MORB + Sulfide 04	Graphite	Sulfide liquid + Silicate melt
BM1–15	1	1500	10 h	MORB + Sulfide 04	Graphite	Sulfide liquid + Silicate melt
BM1–16	1	1600	3 h	MORB + Sulfide 04	Graphite	Sulfide liquid + Silicate melt
BM1–17	1	1700	2 h	MORB + Sulfide 04	Graphite	Sulfide liquid + Silicate melt
BM1–18	1	1800	40 min	MORB + Sulfide 04	Graphite	Sulfide liquid + Silicate melt
BM4–21	4	2100	15 min	MORB + Sulfide 04	Graphite	Sulfide liquid + Silicate melt
BM7–21	7	2100	15 min	Pyrolite + Sulfide 04	Graphite	Sulfide liquid + Silicate melt
BM12–21	12	2100	15 min	MORB + Sulfide 05	MgO	Sulfide liquid + Silicate melt
ZD18	14	2100	15 min	Y98 Silicate + Sulfide 06	MgO	Sulfide liquid + Silicate melt
ZD09	1	1800	30 min	Pyrolite + Sulfide 01	Graphite	Sulfide liquid + Silicate melt
ZD10	3	1700	2 h	Pyrolite + Sulfide 01	Graphite	Sulfide liquid + Silicate melt
ZD11	5	2000	20 min	Pyrolite + Sulfide 01	Graphite	Sulfide liquid + Silicate melt
ZD14	8	2100	15 h	Pyrolite + Sulfide 01	Graphite	Sulfide liquid + Silicate melt
D04	1	1700	2 h	Pyrolite + Sulfide 03	Graphite	Sulfide liquid + Silicate melt
D05	1	1800	30 min	Pyrolite + Sulfide 03	Graphite	Sulfide liquid + Silicate melt
BP1–17	1	1700	2 h	Pyrolite + Sulfide 04	Graphite	Sulfide liquid + Silicate melt
BP1–18	1	1800	40 min	Pyrolite + Sulfide 04	Graphite	Sulfide liquid + Silicate melt
BP3–17	3	1700	2 h	Pyrolite + Sulfide 04	Graphite	Sulfide liquid + Silicate melt
BP3–18	3	1800	40 min	Pyrolite + Sulfide 04	Graphite	Sulfide liquid + Silicate melt
BP4–21	4	2100	15 min	Pyrolite + Sulfide 04	Graphite	Sulfide liquid + Silicate melt
BP7–21	7	2100	15 min	Pyrolite + Sulfide 04	Graphite	Sulfide liquid + Silicate melt

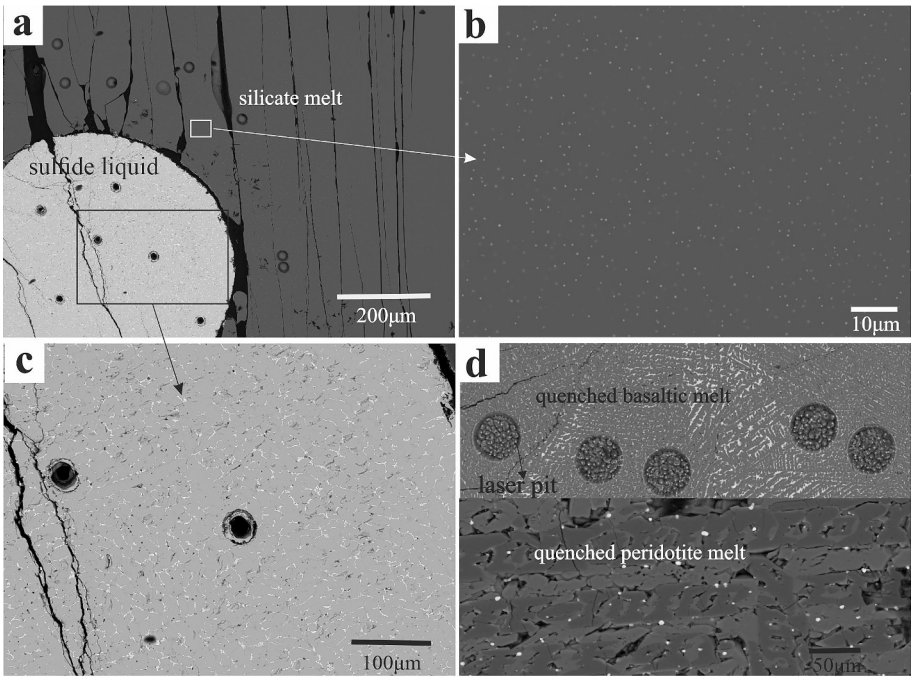

Fig. 1. Selected back-scattered electron (BSE) images showing characteristic features of the run products from sulfide liquid–silicate melt partitioning experiments. (a) BSE image of run D01 (1 GPa and 1600 °C) showing coexisting sulfide liquid and silicate melt in a graphite capsule. (b) Closer view of the quenched silicate melt in (a) showing homogeneously distributed small sulfide dots produced during quenching. (c) Closer view of the quenched sulfide liquid in (a), which includes Fe-rich monosulfide solid solution and chalcopyrite. (d) Closer view of the quenched basaltic melt from run ZD13 at 8 GPa and 2100 °C and peridotitic melt from run BP7–21 at 7 GPa and 2100 °C.

wt% MgO, 4.9–7.8 wt% FeO_{tot}, and 3.8–6.0 wt% CaO. The silicate melt from an experiment starting with Y98 silicate (run ZD18) contains 46.3 wt% SiO_2, 3.5 wt% Al_2O_3, 28.2 wt% MgO, 13.2 wt% FeO_{tot}, and 4.8 wt% CaO. The silicate melts from runs ZD18 and BM12–21 contain significantly more MgO but less FeO, SiO_2, and CaO compared to the starting silicates (Y98 silicate and MORB, respectively) due to the dissolution of the MgO capsules in the silicate melts. The silicate melt NBO/T values (non-bridging oxygens to tetrahedral cations) are ~0.7–1.0 in the experiments starting with MORB, ~2.2–2.6 in the experiments starting with peridotite, and ~ 2.2–3.3 in runs BM12–21 and ZD18 (Table 3).

The time-resolved LA–ICP–MS signals of Re and other trace elements in the silicate melts are smooth and constant, demonstrating that there was no contamination of the silicate melts by sulfide liquid nuggets during the analyses. Most of the trace elements are well above the detection limit of our LA–ICP–MS and are homogeneously distributed in the silicate melts. The trace element concentrations of the silicate melts are ~13–200 μg/g for Pb, 0.3–25 μg/g for Co, 0.8–780 μg/g for Cu, 0.1–980 μg/g for Ni, 20–180 μg/g for Zn, 2.5–310 μg/g for Mo, 3.5–15 μg/g for Ag, 2–57 μg/g for Sb, 0.5–13 μg/g for Bi, 15–590 μg/g for In, 35–160 μg/g for Ge, 57–330 μg/g for Ga, and 3–26 μg/g for Cd. The Re concentrations in silicate melts are ~0.03–0.39 μg/g, which are also significantly above the detection limits of our LA–ICP–MS (~1–3 ng/g).

3.3. Major and trace element compositions of the sulfide liquids

The major and trace element compositions of the sulfide liquids are given in Tables 5 and 6. The sulfide liquids contain 33.0–36.4 wt% S, 50.5–62.5 wt% Fe, 0–7.6 wt% Cu, 0–7.3 wt% Ni, and 0.8–3.4 wt% O. All trace elements analyzed in the sulfide liquids are well above the detection limits. Most trace elements are homogeneously distributed in the sulfide liquids at the scale of our applied laser beam sizes (30–50 μm), except that a few elements in the sulfide liquids of some runs have relatively large uncertainties (e.g., 98 ± 24 μg/g Ni in run BP1–18; 1071 ± 201 μg/g Bi in run BP3–18; Table 6). The trace element concentrations of the sulfide liquids are ~17–850 μg/g for Co, 10–1200 μg/g for Zn, 560–5400 μg/g for Mo, 330–1600 μg/g for Ag, 270–1500 μg/g for Sb, 320–3300 μg/g for In, 540–2200 μg/g for Bi, 90–490 μg/g for Ge, 6–53 μg/g for Ga, 160–550 μg/g for Cd, 420–2800 μg/g for Pb, and 440–2200 μg/g for Re.

3.4. Sulfide liquid–silicate melt partition coefficients of CSEs ($D_{CSE}^{Sul/Sil}$)

The sulfide liquid–silicate melt partition coefficients ($D_{CSE}^{Sul/Sil}$) for Co, Ni, Cu, Zn, Ga, Ge, Mo, Ag, Cd, In, Sb, Re, Pb, and Bi were calculated from their weight fractions in the respective phases and are given in Table 7 and plotted in Figs. 3–7. At the conditions presently studied, $D_{CSE}^{Sul/Sil}$ vary by 1–2 orders of magnitude; $D_{CSE}^{Sul/Sil}$ are between 10^3 and 10^4 for Re; 10^2–10^3 for Bi, Cu, Ni, and Ag; 10–10^2 for Co, Pb, Mo, Cd, and In; 1–10 for Zn and Ge; and < 1 for Ga. Intercorrelations were observed for the $D_{CSE}^{Sul/Sil}$ of some elements. For example, as illustrated in Fig. 3a, regardless of the silicate melt composition, $D_{Cu}^{Sul/Sil}$ and $D_{Ag}^{Sul/Sil}$ are correlated and the $D_{Cu}^{Sul/Sil}/D_{Ag}^{Sul/Sil}$ ratios have an average value of 1.0 ± 0.18. These observations are consistent with previous results obtained in the sulfide liquid–basaltic to rhyolitic melt systems and imply similar partitioning behavior of Cu and Ag (Li et al., 2021). Fig. 3b–d respectively shows that $D_{Bi}^{Sul/Sil}$ and $D_{Ni}^{Sul/Sil}$ are correlated, but $D_{Bi}^{Sul/Sil}$ are moderately higher than $D_{Ni}^{Sul/Sil}$; $D_{Zn}^{Sul/Sil}$ and $D_{In}^{Sul/Sil}$ are correlated, but $D_{In}^{Sul/Sil}$ are moderately higher than $D_{Zn}^{Sul/Sil}$; $D_{Ga}^{Sul/Sil}$ and $D_{Ge}^{Sul/Sil}$ are correlated, but $D_{Ge}^{Sul/Sil}$ are moderately higher than $D_{Ga}^{Sul/Sil}$.

The most important parameters governing $D_{CSE}^{Sul/Sil}$ include pressure, temperature, and/or the silicate melt composition (mainly the FeO_{tot} content of the silicate melt), but the effect of each of these parameters can be very different for a different CSE (Kiseeva and Wood, 2013; Kiseeva and Wood, 2015; Li and Audétat, 2015; Li et al., 2021). In Figs. 4–6, for a given CSE, we have only plotted its $D_{CSE}^{Sul/Sil}$ as a function of a parameter that appears to have the most significant effect on the

Table 3
Major and minor element compositions of the quenched silicate melts (in wt% if not noted).

Run. No	SiO_2	1-σ	TiO_2	1-σ	Al_2O_3	1-σ	FeO_{tot}	1-σ	MgO	1-σ	CaO	1-σ	MnO	1-σ	Na_2O	1-σ	K_2O	1-σ	P_2O_5	1-σ	Cr_2O_3	1-σ	S(μg/g)	1-σ	NBO/T	Total	1-σ
ZD01	50.6	0.4	0.9	0.03	15.5	0.3	7.5	0.1	8.5	0.12	11.4	0.04	0.176	0.027	3.0	0.03	0.12	0.02	0.01	0.01	0.03	0.02	2041	482	0.7	97.6	0.1
ZD02	50.7	0.2	0.9	0.03	15.4	0.2	6.8	0.5	8.9	0.18	11.8	0.16	0.146	0.011	3.2	0.09	0.10	0.02	0.02	0.02	0.02	0.02	2546	501	0.7	98.0	0.1
ZD03	49.9	0.2	0.9	0.03	16.7	0.1	6.3	0.2	9.5	0.08	11.2	0.07	0.159	0.019	3.0	0.06	0.10	0.01	0.02	0.02	0.02	0.02	2845	113	0.7	97.9	0.1
ZD04	51.1	0.3	0.9	0.05	15.7	0.1	8.1	0.3	9.0	0.05	10.8	0.06	0.170	0.026	3.2	0.11	0.10	0.01	0.00	0.00	0.05	0.03	3118	387	0.7	99.0	0.1
ZD05	50.5	0.4	0.9	0.04	15.1	0.2	6.5	0.2	9.1	0.24	11.3	0.04	0.208	0.030	3.4	0.18	0.09	0.01	0.02	0.02	0.02	0.02	3238	676	0.7	97.1	0.1
ZD07	49.1	0.2	0.9	0.04	15.6	0.1	8.8	0.1	8.4	0.14	11.2	0.04	0.175	0.030	3.0	0.04	0.11	0.02	0.02	0.02	0.03	0.01	2270	593	0.7	97.1	0.1
ZD08	49.8	0.2	0.9	0.00	16.6	0.1	7.0	0.4	10.2	0.05	11.4	0.09	0.170	0.001	2.8	0.04	0.11	0.02	0.01	0.00	0.02	0.01	4148	567	0.7	98.9	0.1
ZD13	51.1	0.6	0.5	0.13	15.6	0.5	6.8	0.4	10.3	0.90	11.2	0.94	0.154	0.019	3.2	0.33	0.03	0.02	0.02	0.01	0.04	0.04	2713	835	0.7	98.8	0.3
ZD15	49.1	0.8	1.0	0.02	16.4	0.4	8.7	0.4	8.3	0.09	10.7	0.14	0.180	0.003	2.8	0.03	0.09	0.00	0.01	0.00	0.03	0.02	2280	256	0.7	97.2	0.2
ZD16	48.2	0.7	0.9	0.09	17.7	0.2	8.4	0.2	8.8	0.14	10.1	0.26	0.124	0.024	2.5	0.11	0.08	0.02	0.02	0.02	0.01	0.01	2719	304	0.7	96.7	0.2
ZD17	48.5	0.6	0.6	0.10	16.5	0.2	9.5	0.4	9.1	0.86	10.4	0.57	0.075	0.031	2.6	0.13	0.01	0.01	0.01	0.01	0.02	0.02	2372	396	0.8	97.2	0.3
D01	51.1	0.3	1.0	0.01	15.4	0.2	6.6	0.2	8.9	0.07	11.3	0.07	0.194	0.022	3.2	0.05	0.11	0.01	0.01	0.01	0.03	0.03	3384	581	0.7	97.6	0.1
D02	50.1	0.3	0.9	0.03	15.2	0.2	6.3	0.2	11.8	0.43	11.4	0.10	0.158	0.041	3.3	0.12	0.11	0.01	0.02	0.02	0.02	0.01	3631	786	0.8	99.2	0.1
D03	51.0	0.3	1.0	0.04	15.4	0.1	7.2	0.7	8.9	0.17	11.2	0.13	0.173	0.018	3.2	0.11	0.10	0.01	0.02	0.02	0.04	0.03	3793	1811	0.7	98.2	0.2
BM1–13	50.0	0.5	0.8	0.02	15.7	0.1	8.7	0.1	7.9	0.16	11.2	0.18	0.172	0.012	2.9	0.10	0.09	0.01	0.01	0.02	0.03	0.01	1673	57	0.7	97.4	0.1
BM1–14	50.6	0.2	0.8	0.03	15.6	0.1	8.6	0.1	7.9	0.14	11.2	0.13	0.158	0.014	3.0	0.09	0.10	0.02	0.02	0.02	0.02	0.01	1833	85	0.7	97.8	0.1
BM1–15	50.0	0.2	0.8	0.02	16.2	0.1	8.7	0.1	7.7	0.09	11.4	0.05	0.157	0.014	2.9	0.08	0.10	0.01	0.01	0.01	0.01	0.01	3238	123	0.7	97.9	0.1
BM1–16	50.8	0.2	0.8	0.03	15.7	0.1	8.7	0.1	7.9	0.11	11.3	0.13	0.151	0.013	3.0	0.09	0.09	0.02	0.02	0.01	0.01	0.01	4097	521	0.7	98.4	0.1
BM1–17	51.2	0.4	0.8	0.04	15.6	0.1	8.8	0.3	7.9	0.20	11.0	0.20	0.159	0.014	3.0	0.05	0.08	0.01	0.01	0.02	0.02	0.01	4690	1202	0.7	98.6	0.1
BM1–18	50.2	0.4	0.8	0.07	15.7	0.1	8.7	0.4	7.5	0.81	11.5	0.16	0.159	0.019	2.9	0.35	0.10	0.03	0.02	0.02	0.02	0.01	5280	1040	0.6	97.6	0.2
BM4–21	47.4	0.4	0.7	0.02	14.7	0.1	6.9	0.5	13.6	0.18	12.4	0.13	0.086	0.014	2.2	0.12	0.08	0.02	0.02	0.02	0.01	0.01	6280	1520	1.0	98.0	0.2
BM7–21	48.8	1.8	0.6	0.23	13.6	1.3	6.4	0.5	14.8	1.78	12.2	0.83	0.103	0.015	2.2	0.36	0.02	0.01	0.01	0.01	0.01	0.01	1960	480	1.0	98.7	0.7
BM12–21	38.2	0.6	0.5	0.12	4.5	0.6	3.9	0.6	42.2	1.23	7.0	0.69	0.010	0.002	2.6	0.37	0.03	0.01	0.02	0.00	0.14	0.01	1200	360	3.3	99.1	0.4
ZD18	46.3	1.0	0.4	0.09	3.5	0.3	13.2	1.0	28.2	1.32	4.8	0.26	0.350	0.120	1.5	0.21	0.09	0.01	0.12	0.01	0.22	0.01	1160	160	2.2	98.5	0.4
ZD09	44.6	0.2	0.2	0.00	4.7	0.0	4.9	0.6	38.3	0.28	4.7	0.08	0.009	0.001	0.6	0.02	0.09	0.02	0.01	0.00	0.16	0.03	3998	683	2.5	98.1	0.2
ZD10	44.4	1.0	0.3	0.04	5.8	0.6	7.8	0.1	32.9	1.33	5.1	0.47	0.003	0.005	0.4	0.04	0.09	0.03	0.02	0.01	0.16	0.03	2563	432	2.2	96.9	0.4
ZD11	47.6	1.2	0.2	0.04	7.1	0.5	5.9	0.4	34.8	1.21	3.8	0.55	0.034	0.020	0.3	0.12	0.02	0.01	0.02	0.01	0.03	0.02	3450	503	2.2	99.9	0.4
ZD14	44.1	1.3	0.2	0.07	5.0	0.4	6.6	0.3	35.9	1.05	4.5	0.12	0.017	0.014	0.6	0.16	0.07	0.02	0.01	0.01	0.08	0.03	2906	764	2.5	97.1	0.4
D04	44.6	1.3	0.2	0.12	4.8	0.4	6.4	0.5	37.9	1.90	3.8	0.86	0.015	0.016	0.5	0.30	0.05	0.03	0.01	0.01	0.17	0.03	3963	941	2.5	98.3	0.6
D05	46.3	0.5	0.2	0.01	4.7	0.2	4.9	0.2	36.2	0.48	4.9	0.15	0.014	0.011	0.8	0.07	0.08	0.01	0.01	0.01	0.05	0.01	4227	685	2.4	98.2	0.2
BP1–17	43.2	1.4	0.3	0.02	5.4	0.8	6.3	0.6	35.2	1.34	5.2	0.43	0.011	0.014	2.6	0.08	0.08	0.04	0.03	0.01	0.19	0.04	3840	920	2.4	98.3	0.5
BP1–18	45.5	0.6	0.2	0.02	5.5	0.3	7.3	0.2	32.9	1.00	5.0	0.29	0.012	0.010	2.5	0.12	0.07	0.02	0.01	0.01	0.16	0.03	5640	840	2.4	99.2	0.3
BP3–17	42.5	2.0	0.2	0.07	6.5	0.3	7.4	0.6	34.7	1.13	5.2	0.75	0.010	0.012	2.0	0.23	0.06	0.03	0.01	0.01	0.15	0.02	3520	640	2.5	98.7	0.6
BP3–18	44.8	1.7	0.1	0.10	5.0	0.4	6.3	0.4	35.3	1.71	4.1	0.68	0.021	0.006	2.2	0.96	0.04	0.03	0.01	0.01	0.15	0.02	2840	520	2.3	97.9	0.6
BP4–21	43.2	0.6	0.1	0.02	5.7	0.7	7.2	0.5	35.8	1.39	4.5	0.62	0.001	0.002	3.2	0.42	0.04	0.01	0.02	0.01	0.11	0.01	4520	1080	2.6	99.8	0.4
BP7–21	42.1	0.7	0.4	0.14	6.2	0.5	6.1	0.4	35.9	0.01	6.0	0.07	0.005	0.001	2.7	0.36	0.01	0.02	0.03	0.01	0.14	0.02	1520	480	2.6	99.5	0.2

For each sample, 10–15 spots were analyzed by EPMA, and 1-σ is the standard deviation based on the replicate analyses.

Table 4
Trace element compositions of the quenched silicate melts (in μg/g).

Run. No	Pb	1-σ	Co	1-σ	Ni	1-σ	Cu	1-σ	Zn	1-σ	Mo	1-σ	Ag	1-σ	Sb	1-σ	Re	1-σ	Bi	1-σ	In	1-σ	Ge	1-σ	Ga	1-σ	Cd	1-σ
ZD01					24	5	81	16			15	1.0					0.03	0.01										
ZD02					26	3	107	29			15	0.4					0.03	0.01										
ZD03					29	0.5	134	6			10	0.2					0.03	0.01										
ZD04					39	1	270	4			8	0.1					0.07	0.01										
ZD05					41	3	291	15			7	0.1					0.10	0.01										
ZD07					51	3	213	8			13	0.2					0.09	0.01										
ZD08					52	4	387	27			6	0.3					0.09	0.01										
ZD13					114	14	776	87			9	0.4					0.15	0.03										
ZD15					91	5	625	18			13	0.5					0.19	0.02										
ZD16	203	21	22	4	15	2	69	30			10	1.6	12	2			0.11	0.03	7	3	200	8						
ZD17	190	29	25	1	23	2	57	3			14	1.2	15	0.7			0.15	0.06	14	3	592	76						
D01	20	0.2	8	0.4	54	2	38	2	168	2	4.3	0.6	1	0.2	3	0.3			0.49	0.04								
D02	19	0.3	9	0.3	73	9	72	8	117	3	3.2	0.4	3	0.2	2	0.2			0.58	0.03								
D03	23	0.8	13	1	102	13	108	9	97	3	3.1	0.2	3	0.3	2	0.1			0.75	0.12								
BM1–13	17	0.6	0.30	0.01	0.25	0.07			59	1					57	0.5			1.7	0.3	27	0.2	140	1	121	2	4	0.1
BM1–14	24	0.6	0.30	0.02	0.31	0.05			23	0					43	0.9			2.1	0.2	30	0.2	135	1	90	1	4	0.1
BM1–15	26	0.1	0.35	0.01	0.27	0.02			130	3					31	0.6			1.8	0.0	29	0.2	93	1	65	1	6	0.3
BM1–16	24	0.6	0.36	0.02	0.39	0.06			22	0.4					26	0.2			2.2	0.2	29	0.3	76	0	58	0	5	0.1
BM1–17	26	0.4	0.40	0.01	0.38	0.05			23	1					23	0.4			2.4	0.1	26	0.4	72	1	87	1	6	0.2
BM1–18	25	0.6	0.43	0.02	0.56	0.04			20	1					17	0.6			2.7	0.3	33	0.6	59	5	72	8	7	0.2
BM4–21	17	2.5	0.34	0.09	0.55	0.12			28	2					15	2			2.3	0.5	27	1	56	2	123	3	11	2
BM7–21	50	3.9	0.32	0.03	0.73	0.12			92	4					39	4			6.2	1.2	140	8	35	6	331	14	26	2
BM12–21	16	3.1	0.24	0.05	1.5	0.2	0.8	0.2	27	0.3	2.5	0.2			13	2			3.1	1.0	71	4	75	2	57	3	7	0.4
ZD18	38	3.7	0.81	0.01	984	102	535	32	31	1	305	55	32	10	20	5	0.39	0.11	11	2	93	11	164	12	265	12	19	5
ZD09					51	6	377	42			4	0.7					0.09	0.02										
ZD10					71	8	380	24			18	2					0.18	0.04										
ZD11					90	19	596	57			14	4					0.14	0.05										
ZD14					105	19	737	65			12	0.5					0.17	0.03										
D04	15	1.4	11	1	86	15	78	7	179	17	9.9	1.4	3	0.1	6	0.5			0.45	0.16								
D05	9	5.8	5	2	115	21	103	34	161	8	2.7	0.9	4	0.4	4	1.0			0.61	0.01								
BP1–17	13	1.2	0.31	0.07	0.22	0.03			52	7					18	2			1.9	0.3	15	2	80	6	128	19	3	0.5
BP1–18	17	1.8	0.37	0.09	0.23	0.05			79	2					18	3			2.5	0.5	20	3	77	7	72	5	6	0.6
BP3–17	18	1.5	0.31	0.05	0.13	0.02			73	2					18	2			1.1	0.3	19	2	83	3	123	5	4	0.3
BP3–18	21	2.4	0.36	0.00	0.24	0.03			76	3					19	3			1.8	0.3	25	2	99	3	63	2	7	0.6
BP4–21	7	0.9	0.32	0.05	0.21	0.05			62	1					16	1			3.9	0.4	39	1	79	14	38	5	7	1
BP7–21	49	3.9	0.42	0.06	0.56	0.11			56	3					20	1			5.5	0.5	109	5	118	6	246	9	17	1

For each sample, 8–12 spots were analyzed by LA-ICP-MS, and 1-σ is the standard deviation based on the replicate analyses.

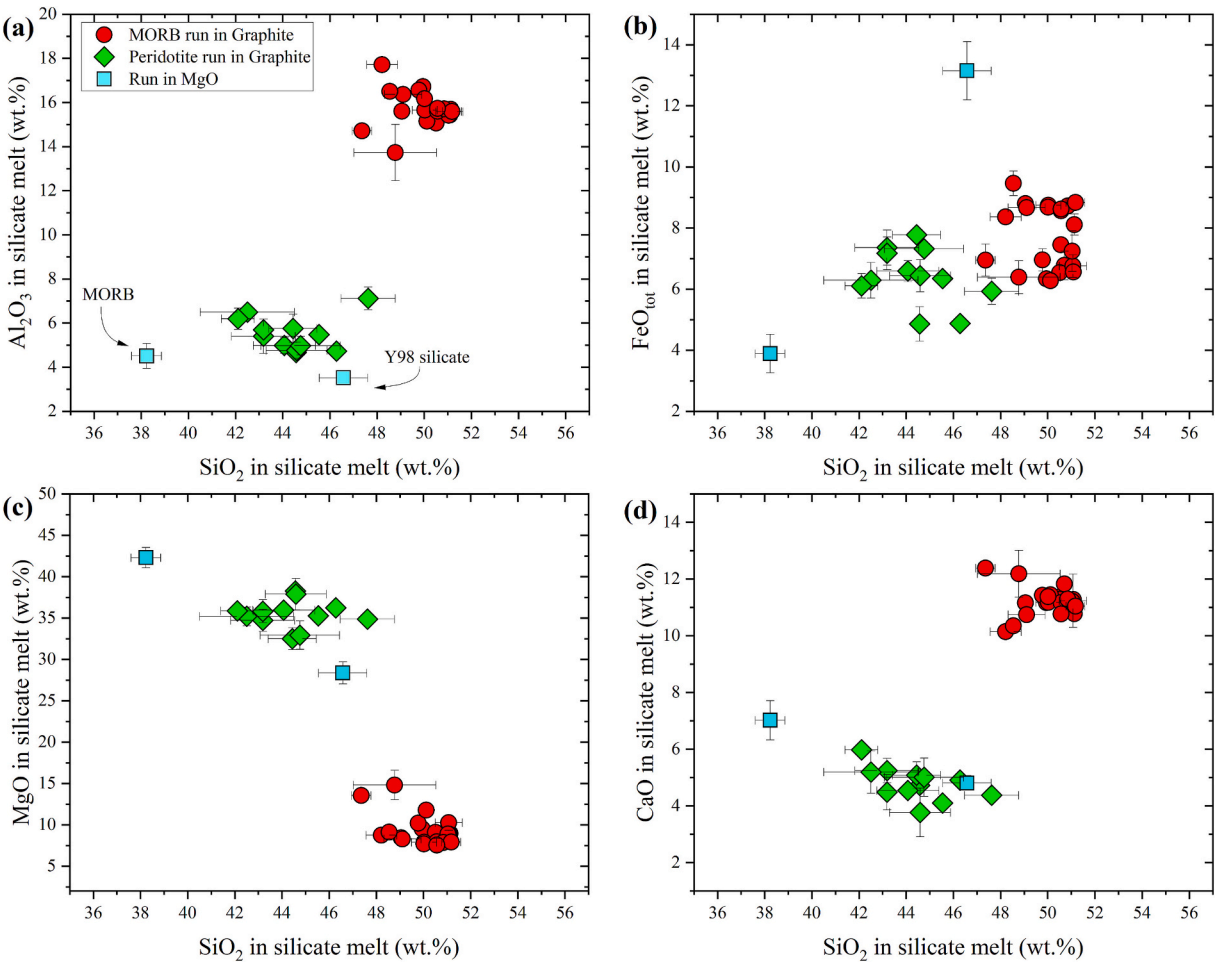

Fig. 2. The major element compositions of the quenched silicate melts as a function of the SiO_2 contents in silicate melts. This figure illustrates the variation in the SiO_2, Al_2O_3, FeO, MgO, and CaO compositions of the silicate melts.

$D_{CSE}^{Sul/Sil}$. Fig. 4 shows that the increase in temperature from 1300 to 2100 °C leads to a significant decrease in the $D_{CSE}^{Sul/Sil}$ for Ni (1200–50), Cu (940–40), Ag (310–50), and Re (30000–4000); however, the $D_{CSE}^{Sul/Sil}$ for Ga (0.05–0.92) and Ge (0.7–6.8) appear to increase with increasing temperature. Fig. 5 shows that the increase in pressure from 1 to 14 GPa also leads to a decrease in the $D_{CSE}^{Sul/Sil}$ for Ni (1200–50), Zn (7–0.5), Bi (1700–130), Cd (87–20), In (60–3), and Cu (940–40). Fig. 6 shows that the decrease in FeO_{tot} content of the silicate melt leads to an increase in the $D_{CSE}^{Sul/Sil}$ for Co (30–160), Mo (20−200), Sb (20–150), Pb (15–210), Bi (130–1700), and Cu (940–40). The scatter of $D_{CSE}^{Sul/Sil}$ in each plot of Figs. 4–6 is due to the fact that the $D_{CSE}^{Sul/Sil}$ are governed by several parameters. For example, the $D_{CSE}^{Sul/Sil}$ for Ni show dependence on both temperature (Fig. 4a) and pressure (Fig. 4d), which means that both parameters can control $D_{Ni}^{Sul/Sil}$. Similarly, the $D_{CSE}^{Sul/Sil}$ for Bi are controlled by both temperature (Fig. 5b) and the FeO_{tot} content of the silicate melt (Fig. 6a). It should be also noted that as illustrated in Figs. 4–6, the $D_{CSE}^{Sul/Sil}$ obtained from the sulfide liquid–peridotitic melt system and the $D_{CSE}^{Sul/Sil}$ obtained from the sulfide liquid–basaltic melt system are consistent, and they follow the effects of pressure, temperature, and FeO_{tot} content of the silicate melt in a similar manner. Furthermore, $D_{Re}^{Sul/Sil}$ appear to increase with pressure (Fig. 4d), although the increase in temperature clearly leads to a reduction in $D_{Re}^{Sul/Sil}$. $D_{Re}^{Sul/Sil}$ and $D_{Cu}^{Sul/Sil}$ share a similar temperature-dependence, as evidenced by the data at pressures lower than 4 GPa (Fig. 4b, d). However, the $D_{Re}^{Sul/Sil}/D_{Cu}^{Sul/Sil}$ ratios, ranging from 29 to 106, were observed to be strongly pressure-dependent (Fig. 7), which indicates that pressure may exert a positive influence on $D_{Re}^{Sul/Sil}$. In the following section, the effects of different parameters on $D_{CSE}^{Sul/Sil}$ will be further considered in a quantitative manner.

4. Discussion

4.1. Comparison with previous data and parameterization of $D_{CSE}^{Sul/Sil}$

Despite the fact that all available $D_{CSE}^{Sul/Sil}$ were obtained in the sulfide liquid–rhyolitic to peridotitic systems, the present observations of the effects of temperature, pressure, and FeO_{tot} content of the silicate melt on $D_{CSE}^{Sul/Sil}$ are systematically and qualitatively consistent with the results obtained from previous experiments conducted at pressures ≤3 GPa and temperatures ≤1700 °C (Fig. 8). For example, our $D_{Cu,Ag}^{Sul/Sil}$, together with previous data (Brenan, 2008; Kiseeva and Wood, 2013; Kiseeva and Wood, 2015; Li and Audétat, 2012; Li and Audétat, 2015; Li et al., 2021; Mungall and Brenan, 2014), demonstrate a decline with rising temperature and FeO_{tot} content of the silicate melt (Fig. 8a-b); our $D_{Bi,Ni}^{Sul/Sil}$, together with previous data (Gaetani and Grove, 1997; Kiseeva and Wood, 2013; Kiseeva and Wood, 2015; Li and Audétat, 2012; Li and Audétat, 2015; Peach and Mathez, 1993), demonstrate a decline with rising pressure (Fig. 8c-d). Furthermore, our $D_{Co,Ni}^{Sul/Sil}$, together with previous data (Gaetani and Grove, 1997; Kiseeva and Wood, 2013; Kiseeva

Table 5
Major element compositions of the sulfide liquids (in wt%).

Run. No	Fe	1-σ	S	1-σ	O	1-σ	Ni	1-σ	Cu	1-σ	Total	1-σ
ZD01	53.1	2.2	34.1	0.7	1.9	0.7	3.0	0.1	7.6	0.7	99.7	0.7
ZD02	52.2	1.4	34.3	0.3	2.0	0.5	3.0	0.0	7.7	0.2	99.2	0.5
ZD03	53.9	1.3	35.0	1.2	1.1	0.4	3.2	0.1	6.3	0.8	99.5	0.5
ZD04	54.3	1.5	33.6	0.5	1.6	0.5	2.8	0.1	6.6	0.7	99.0	0.5
ZD05	55.0	1.1	34.1	0.7	1.1	0.4	2.9	0.0	6.7	0.5	99.7	0.4
ZD07	52.7	0.7	34.8	0.5	1.3	0.4	3.5	0.0	6.7	0.3	99.0	0.2
ZD08	53.7	1.3	33.9	1.5	1.3	0.4	3.3	0.1	7.5	0.6	99.7	0.5
ZD13	52.7	0.4	35.9	0.3	1.3	0.2	3.2	0.1	6.4	0.2	99.6	0.1
ZD15	51.5	1.6	34.4	0.6	2.5	0.4	2.5	0.1	6.6	0.3	97.5	0.5
ZD16	59.4	0.3	35.6	0.8	1.9	0.1	0.4	0.0	0.5	0.0	97.9	0.3
ZD17	59.7	0.4	35.5	0.4	3.4	0.7	0.4	0.0	0.3	0.0	99.3	0.3
D01	58.3	0.4	33.7	0.5	1.6	0.2	4.6	0.4	1.4	0.1	99.5	0.2
D02	56.5	0.7	34.0	0.5	1.2	0.3	5.3	0.2	1.9	0.1	99.0	0.2
D03	56.5	0.6	33.7	1.0	1.8	0.7	6.0	0.2	1.7	0.1	99.6	0.3
BM1–13	61.5	0.6	35.1	0.9	1.9	0.9					98.5	0.4
BM1–14	61.5	0.6	34.3	0.9	2.6	0.9					98.4	0.4
BM1–15	61.5	0.4	34.3	1.2	2.6	0.4					98.5	0.4
BM1–16	62.5	0.4	35.4	0.9	2.0	1.0					99.8	0.4
BM1–17	61.9	0.6	34.8	0.9	2.1	0.9					98.9	0.4
BM1–18	61.9	0.6	34.6	0.8	2.1	0.6					98.7	0.3
BM4–21	61.7	0.5	35.7	0.6	1.5	0.5					98.8	0.2
BM7–21	61.7	0.3	35.2	0.5	1.3	0.4					98.2	0.2
BM12–21	60.3	0.3	36.4	0.3	0.8	0.1					97.4	0.1
ZD18	56.6	0.5	34.1	0.3	1.0	0.2	4.5	0.4	2.9	0.1	99.0	0.1
ZD09	53.8	0.3	33.2	0.5	1.4	0.5	3.3	0.2	7.4	1.2	99.1	0.4
ZD10	50.5	2.2	33.2	1.1	2.4	0.9	3.3	0.1	7.2	0.9	96.5	0.7
ZD11	51.4	0.7	34.7	0.7	1.8	0.3	3.3	0.0	7.0	0.2	98.2	0.3
ZD14	52.5	0.5	35.5	0.6	1.3	0.5	3.3	0.1	6.4	0.2	99.0	0.2
D04	54.8	0.9	33.7	1.1	1.6	0.5	7.3	0.3	2.2	0.2	99.5	0.3
D05	54.4	1.7	34.3	1.6	1.6	0.2	6.8	0.5	1.9	0.2	99.0	0.7
BP1–17	61.3	0.3	33.0	0.1	1.6	0.1					95.9	0.1
BP1–18	60.8	0.2	34.9	0.1	2.0	0.1					97.7	0.1
BP3–17	61.4	0.3	36.3	0.4	1.4	0.4					99.2	0.2
BP3–18	61.5	0.3	35.0	1.1	1.3	0.2					97.9	0.4
BP4–21	61.4	0.6	34.5	1.3	2.0	0.6					98.0	0.5
BP7–21	61.7	0.7	35.1	1.1	1.5	0.6					98.3	0.4

For each sample, 10–15 spots were analyzed by EPMA, and 1-σ is the standard deviation based on the replicate analyses.

and Wood, 2015; Li and Audétat, 2012; Li and Audétat, 2015; Li et al., 2021; Peach and Mathez, 1993), demonstrate a decline with rising FeO_{tot} content of the silicate melt (Fig. 8e-f).

Previous authors (Kiseeva and Wood, 2013; Kiseeva and Wood, 2015; Li and Audétat, 2015; Li et al., 2021) have demonstrated that the large variation in $D_{CSE}^{Sul/Sil}$ can be explained by a partitioning model, which describes $D_{CSE}^{Sul/Sil}$ as a function of multiple variables, including pressure, temperature, composition of the silicate melt and sulfide liquid, and fO_2 for the elements with multiple valence states. The following equation is used to represent the model:

$$\begin{aligned} logD_{CSE}^{Sul/Sil} = {} & C + \frac{a}{T} + b\cdot\frac{P}{T} + c\cdot log\left[X_{FeO_{tot}}^{Sil}\right]_{corr} + d \bullet \Delta FMQ \\ & + 1673\Big/T\cdot\left[\varepsilon_{CSE}^{FeO}\cdot log\left(1-x_{FeO}^{Sul}\right) + \varepsilon_{CSE}^{NiS}\cdot log\left(1-x_{NiS}^{Sul}\right)\right. \\ & \left. + \varepsilon_{CSE}^{CuS_{0.5}}\cdot log\left(1-x_{CuS_{0.5}}^{Sul}\right] + \sum e_i\cdot log x_i^{Sil}\right. \end{aligned} \quad (1)$$

where T is temperature in K; P is pressure in GPa; ε_{CSE}^{FeO}, ε_{CSE}^{NiS} and $\varepsilon_{CSE}^{CuS_{0.5}}$ represent non-idea interaction parameters between a CSE and the sulfide liquid composition; ΔFMQ is fO_2 relative to the FMQ buffer; x_{FeO}^{Sul}, x_{NiS}^{Sul}, $x_{CuS_{0.5}}^{Sul}$ are mole fractions of FeO, NiS, and $CuS_{0.5}$ in the sulfide liquid; x_i^{Sil} is mole fraction of an oxide in the silicate melt; C is a constant; and $\left[X_{FeO_{tot}}^{Sil}\right]_{corr}$ is the total Fe oxides in the silicate melt (wt%) corrected for the ideal activity of FeS in the sulfide liquid (Kiseeva and Wood, 2015; Li et al., 2021):

$$\left[X_{FeO_{tot}}^{Sil}\right]_{corr} = \frac{X_{FeO_{tot}}^{Sil}}{\left[x_{Fe}^{Sul}\Big/\left(x_{Fe}^{Sul}+x_{Ni}^{Sul}+x_{Cu}^{Sul}\right)\right]} \quad (2)$$

The coefficients a, b, c, d, e_i and the constant C in Eq. (1) can be obtained through multiple linear regression fitting of the $D_{CSE}^{Sul/Sil}$ data. The details of the derivation of Eq. (1) are provided in the Supplementary Materials. In the case a CSE exhibits a single valence state or if the experiments are conducted at conditions of a narrow fO_2 range, the term of $d \bullet \Delta FMQ$ in Eq. (1) can be removed, thereby eliminating the influence of fO_2 on $D_{CSE}^{Sul/Sil}$. As demonstrated by Li et al. (2021), Eq. (1) is capable of explaining the large range of observed $D_{CSE}^{Sul/Sil}$ values for a large number of CSEs (Co, Ni, Cu, Zn, As, Mo, Ag, Cd, In, Sn, Sb, W, Re, Pb and Bi) obtained in the sulfide liquid–rhyolitic to basaltic melt systems.

All available $D_{CSE}^{Sul/Sil}$ data were incorporated into Eq. (1), including the present data and the previously published data sets (Table S1) (Brenan, 2008; Brenan, 2015; Feng and Li, 2019; Gaetani and Grove, 1997; Kiseeva and Wood, 2013; Kiseeva and Wood, 2015; Li, 2014; Li and Audétat, 2012; Li and Audétat, 2015; Li et al., 2021; Peach and Mathez, 1993). The utilized $D_{CSE}^{Sul/Sil}$ data were obtained at 1 bar to 14 GPa and 1100 to 2100 °C. The silicate melts contain 0.2–40 wt% FeO, and the sulfide liquids contain 0–45 wt% Cu and 0–59 wt% Ni. However, the $D_{CSE}^{Sul/Sil}$ data obtained at relatively reducing conditions (fO_2 < IW; IW = the Fe–FeO buffer) or oxidizing conditions (fO_2 > FMQ) were excluded for the trace elements with multiple valence states, namely Re, Mo, Sb, and Bi (Brenan, 2008; Feng and Li, 2019; Li et al., 2021; Steenstra et al., 2020a; Steenstra et al., 2020b). The previous $D_{CSE}^{Sul/Sil}$ data for Re, Mo, Sb, and Bi obtained in graphite capsules were utilized exclusively. This is due to the fact that the majority of our experiments were conducted in graphite capsules, and the fO_2 should have been below the C–CO_2 buffer but above the IW buffer (Kiseeva and Wood, 2013; Li and Audétat, 2012). This range of fO_2 is likely to be close proximity to the fO_2 at

Table 6
Trace element compositions of the sulfide liquids (in μg/g).

Run. No	Co	1-σ	Ni	1-σ	Cu	1-σ	Zn	1-σ	Mo	1-σ	Ag	1-σ	Sb	1-σ	Re	1-σ	In	1-σ	Bi	1-σ	Ge	1-σ	Ga	1-σ	Cd	1-σ	Pb	1-σ
ZD01									578	32					878	31												
ZD02									639	30					828	35												
ZD03									607	44					572	45												
ZD04									610	31					725	43												
ZD05									599	33					828	35												
ZD07									655	25					831	34												
ZD08									686	48					649	53												
ZD13									787	14					1071	39												
ZD15									709	14					790	27												
ZD16	846	7							744	20	1165	50			441	7	3324	60	2122	138								
ZD17	757	13							757	19	971	46			573	11	2415	103	1480	68								
D01	651	44					834	79	573	65	328	35	265	61					589	72								
D02	675	16					700	96	568	49	768	110	303	25					676	90								
D03	740	35					874	39	589	28	617	63	297	26					537	74								
BM1–13	18	0.3	166	4			166	14					1196	129			563	76	1454	146	92	9	6	1	314	49	916	97
BM1–14	17	0.6	145	5			75	6					1088	232			730	81	1637	309	143	16	6	1	414	54	1076	106
BM1–15	18	0.4	153	2			401	35					878	82			625	53	1366	138	191	15	10	2	334	44	911	112
BM1–16	18	0.4	154	3			79	6					952	233			806	68	1282	193	247	33	10	2	291	37	795	125
BM1–17	18	0.5	199	6			76	7					1016	114			604	84	1406	198	259	31	20	5	273	32	728	76
BM1–18	19	0.4	187	9			76	6					762	124			788	83	1154	85	333	49	35	10	306	30	626	56
BM4–21	19	1.2	197	5			113	8					1064	147			621	94	1113	119	381	50	52	14	493	74	610	138
BM7–21	17	0.5	45	3			134	15					1108	158			729	87	1983	155	224	52	43	9	411	54	1017	281
BM12–21	18	0.8	76	2	29	4	59	0					988	164			868	66	1459	167	492	30	52	2	290	15	943	139
ZD18	22	0.3					8	2	5370	1169	1598	15	594	36	2202	336	322	53	1528	156	370	32	44	12	347	15	572	124
ZD09									697	96					495	48												
ZD10									688	64					1095	100												
ZD11									774	19					895	20												
ZD14									765	20					1012	23												
D04	854	21					1213	208	572	23	736	39	466	55					747	116								
D05	819	8					817	113	565	83	762	125	451	109					741	193								
BP1–17	16	0	84	3			312	24					1270	183			892	148	1709	133	247	51	33	9	316	22	2759	398
BP1–18	20	1	99	23			499	111					1100	184			778	155	1829	109	357	65	17	6	376	50	1711	251
BP3–17	17	1	54	1			194	11					890	72			289	11	698	100	239	34	22	6	163	12	632	64
BP3–18	22	1	81	5			192	12					1051	118			473	51	1071	201	391	56	20	6	313	41	855	152
BP4–21	19	1	103	5			241	28					1181	181			865	115	1820	112	359	88	12	6	423	53	419	56
BP7–21	29	1	85	3			129	10					1463	164			978	88	2213	213	400	61	37	6	547	43	1988	227

For each sample, 8–12 spots were analyzed by LA-ICP-MS, and 1-σ is the standard deviation based on the replicate analyses.

Table 7
Determined partition coefficients of trace elements between sulfide liquid and silicate melt.

Run. No	D (Mo)	1-σ	D (Re)	1-σ	D (Sb)	1-σ	D (Cu)	1-σ	D (Ag)	1-σ	D (Bi)	1-σ	D (Zn)	1-σ	D (Ni)	1-σ	D (Co)	1-σ	D (Ga)	1-σ	D (Ge)	1-σ	D (Cd)	1-σ	D (Pb)	1-σ	D (In)	1-σ
ZD01	38	6		8761			941	31							1222	148	62	4										
ZD02	42	6		5874			721	27							1149	192	75	4										
ZD03	59	8		7022			467	22							1083	25	85	7										
ZD04	76	9		1701			244	16							727	37	52	3										
ZD05	86	9		1085			231	15							704	29	43	4										
ZD07	51	7		1431			317	18							676	39	39	1										
ZD08	116	11		980			193	14							642	35	49	4										
ZD13	84	9		1398			83	9							286	30	43	4										
ZD15	54	2		389			106	7							273	16	32	1										
ZD16	74	11		475			80	18	97	20	299	131			244	34	39	7										
ZD17	53	10		587			54	19	65	8	109	24			166	72	31	2										
D01	133	25			95	10	360	28	310	60	1194	181	4.9	0.9	854	80	83	7										
D02	176	25			145	12	260	36	280	46	1163	167	6.0	0.8	726	93	73	3										
D03	192	16			132	11	153	15	177	23	717	149	4.9	0.4	586	78	59	4										
BM1–13					21	2					863	155	2.8	0.2	654	180	60	2	0.05	0.01	0.7	0.1	87	14	53	6	21	3
BM1–14					25	5					786	174	3.3	0.3	466	78	58	4	0.07	0.01	1.1	0.1	93	12	46	5	24	3
BM1–15					28	3					761	80	3.1	0.3	561	50	51	2	0.16	0.02	2.0	0.2	56	8	35	4	22	2
BM1–16					37	9					596	102	3.7	0.3	392	56	50	3	0.18	0.03	3.3	0.4	61	8	33	5	28	2
BM1–17					43	5					590	88	3.4	0.3	531	70	46	2	0.23	0.06	3.6	0.4	46	6	28	3	24	3
BM1–18					44	7					433	60	3.8	0.3	331	29	45	3	0.49	0.15	5.6	0.9	47	5	25	2	24	3
BM4–21					72	15					487	128	4.0	0.4	357	78	57	16	0.42	0.12	6.8	0.9	45	9	36	10	23	4
BM7–21					29	5					320	65	1.5	0.2	61	11	55	5	0.13	0.03	6.5	1.9	16	2	21	6	5	1
BM12–21					76	17	37	9			469	161	2.1	0.0	50	5	75	16	0.92	0.06	6.6	0.4	42	3	58	14	12	1
ZD18	18	5		1880	29	8	54	3	50	16	134	31	0.3	0.1	46	6	27	1	0.16	0.04	2.3	0.3	18	5	15	4	3	1
ZD09	175	13		1391			195	14							639	55	65	9										
ZD10	39	6		1336			189	14							457	53	46	5										
ZD11	54	7		2231			118	11							363	87	59	12										
ZD14	63	8		926			87	9							310	43	60	12										
D04	58	9			74	9	283	41	211	46	1661	633	6.8	1.3	846	155	75	7										
D05	207	74			115	11	185	64	191	36	1211	317	5.2	0.8	595	116	160	38										
BP1–17					70	14					886	154	6.0	0.9	381	59	53	12	0.26	0.08	3.1	0.7	94	15	209	36	59	12
BP1–18					61	15					742	157	6.3	1.4	435	143	55	13	0.23	0.08	4.6	1.0	66	11	103	19	39	9
BP3–17					51	7					623	177	2.7	0.2	417	69	54	9	0.18	0.05	2.9	0.4	37	4	35	5	16	1
BP3–18					56	12					582	147	2.5	0.2	336	46	60	4	0.31	0.09	4.0	0.6	42	6	41	9	19	2
BP4–21					73	13					464	58	3.9	0.5	486	126	59	9	0.30	0.16	4.6	1.4	57	9	60	11	22	3
BP7–21					72	9					405	54	2.3	0.2	152	30	71	11	0.15	0.02	3.4	0.5	32	3	41	6	9	1

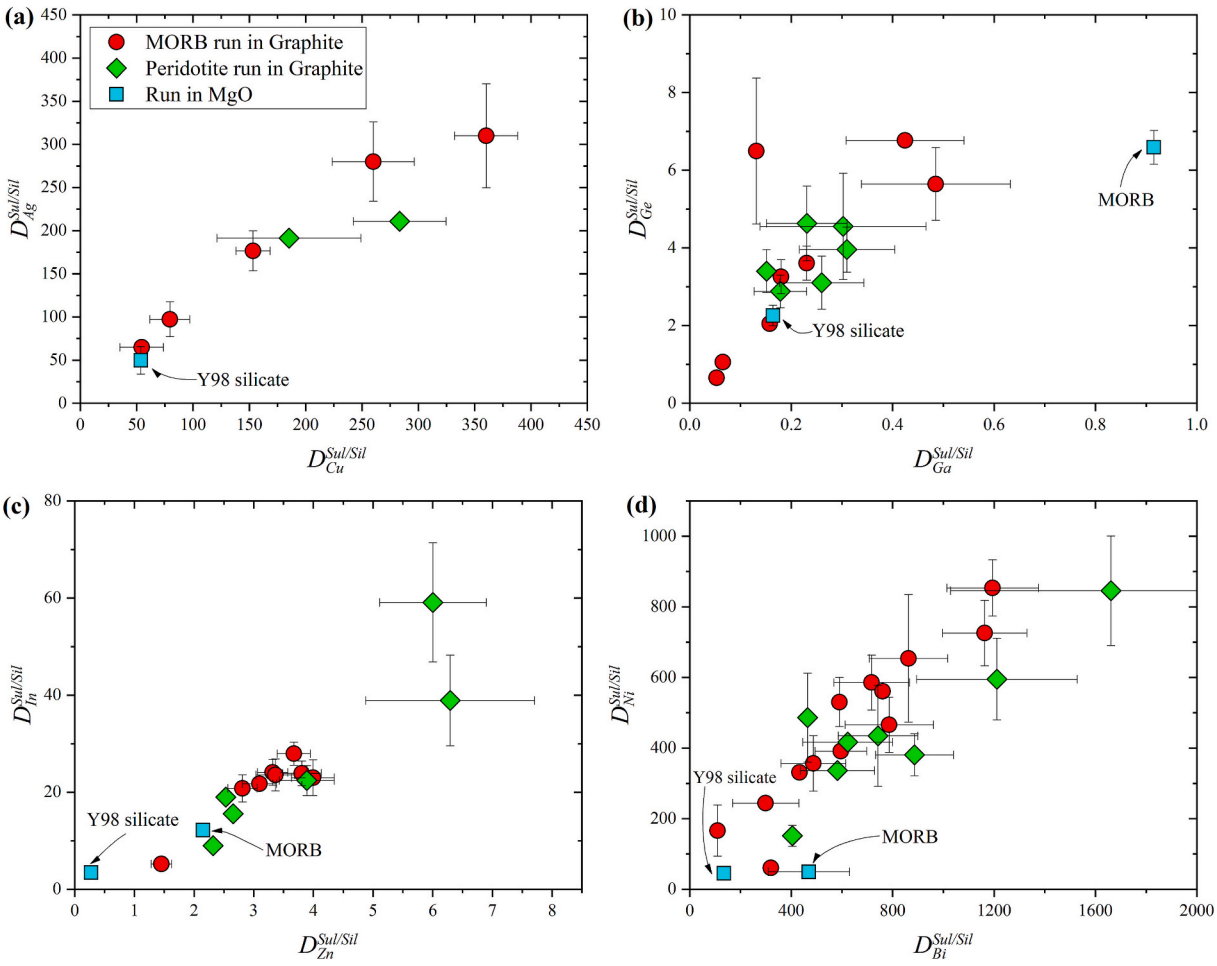

Fig. 3. Correlations between the sulfide liquid–silicate melt partition coefficients of Cu, Ag, Ga, Ge, Zn, In, Bi and Ni. (a) $D_{Cu}^{Sul/Sil}$ vs. $D_{Ag}^{Sul/Sil}$; (b) $D_{Ga}^{Sul/Sil}$ vs. $D_{Ge}^{Sul/Sil}$; (c) $D_{Zn}^{Sul/Sil}$ vs. $D_{In}^{Sul/Sil}$; (d) $D_{Bi}^{Sul/Sil}$ vs. $D_{Ni}^{Sul/Sil}$.

which mantle-to-core segregation of sulfide liquids occurred in the magma ocean (Wood et al., 2006).

The fitting coefficients obtained for Eq. (1) are presented in Table 8. The correlation coefficients (R^2) obtained for all studied CSEs are above 0.86, with 1-sigma standard deviation ranging between 0.09 and 0.37. Figs. S1 and S2 illustrate the correlations between the experimentally determined $D_{CSE}^{Sul/Sil}$ and the predicted values obtained through the application of Eq. (1). These figures demonstrate that Eq. (1) is an effective tool for capturing the full range of experimental data.

The obtained fitting coefficients (Table 8) indicate that an increase in temperature would result in a decrease in the $D_{CSE}^{Sul/Sil}$ for Co, Ni, Cu, Ag, Pb, Cd, Bi, and Re, while an increase in temperature would result in an increase in the $D_{CSE}^{Sul/Sil}$ for Zn, Ga, Ge, In, Mo, and Sb. An increase in pressure would typically result in a decrease in $D_{CSE}^{Sul/Sil}$, but this is not the case for Re, where $D_{Re}^{Sul/Sil}$ are observed to increase with rising pressure, consistent with what we discussed previously. The positive effect of pressure on $D_{Re}^{Sul/Sil}$ is in accordance with the fitting results of Li et al. (2021), and a positive effect of pressure was also observed on the partitioning of Re between monosulfide-solid-solution and silicate melt (Xue and Li, 2021).

The obtained fitting coefficients (Table 8) also indicate that the $D_{CSE}^{Sul/Sil}$ for all studied trace elements increase with a reduction in FeO_{tot} content of the silicate melt. Although all available $D_{CSE}^{Sul/Sil}$ were obtained with silicate melt composition ranging from rhyolite to peridotite, the FeO_{tot} content of the silicate melt is sufficient to describe the effect of the silicate melt composition on $D_{CSE}^{Sul/Sil}$; only $D_{Mo}^{Sul/Sil}$ show some dependence on the Al_2O_3 and CaO content of the silicate melt. The presence of Cu, Ni, and O in sulfide liquids exerts a slight to moderate influence on the $D_{CSE}^{Sul/Sil}$ for certain elements, including Zn, Cu, and Mo (Table 8). In the following section, we will employ Eq. (1) to predict the $D_{CSE}^{Sul/Sil}$ at conditions pertinent to the mantle-to-core segregation of sulfide liquids occurring in a magma ocean.

4.2. *Effect of mantle-to-core segregation of sulfide liquids on CSE abundances of the silicate Earth*

In this section, we utilized Eq. (1) to investigate the influence of mantle-to-core segregation of sulfide liquids on the CSE abundances of the silicate Earth, as postulated by many previous researchers (Ballhaus et al., 2017; Ballhaus et al., 2013; Hart and Gaetani, 2006; Kiseeva and Wood, 2015; O'Neill, 1991; Righter et al., 2018; Rubie et al., 2016; Savage et al., 2015; Wood et al., 2008; Yoshizaki and McDonough, 2021). The presence of immiscible sulfide liquids in the Earth's solidifying magma ocean necessitates that the S concentrations in the silicate magma ocean exceed the sulfur concentration in the silicate melt at sulfide saturation (SCSS), which is a function of pressure, temperature, and composition of the silicate melt and sulfide liquid (Blanchard et al., 2021; Ding et al., 2014; Laurenz et al., 2016; Mavrogenes and O'Neill, 1999; Smythe et al., 2017). Consequently, significant research has been conducted to elucidate the impact of these variables on SCSS and the exsolution of sulfide liquids in the Earth's solidifying magma ocean

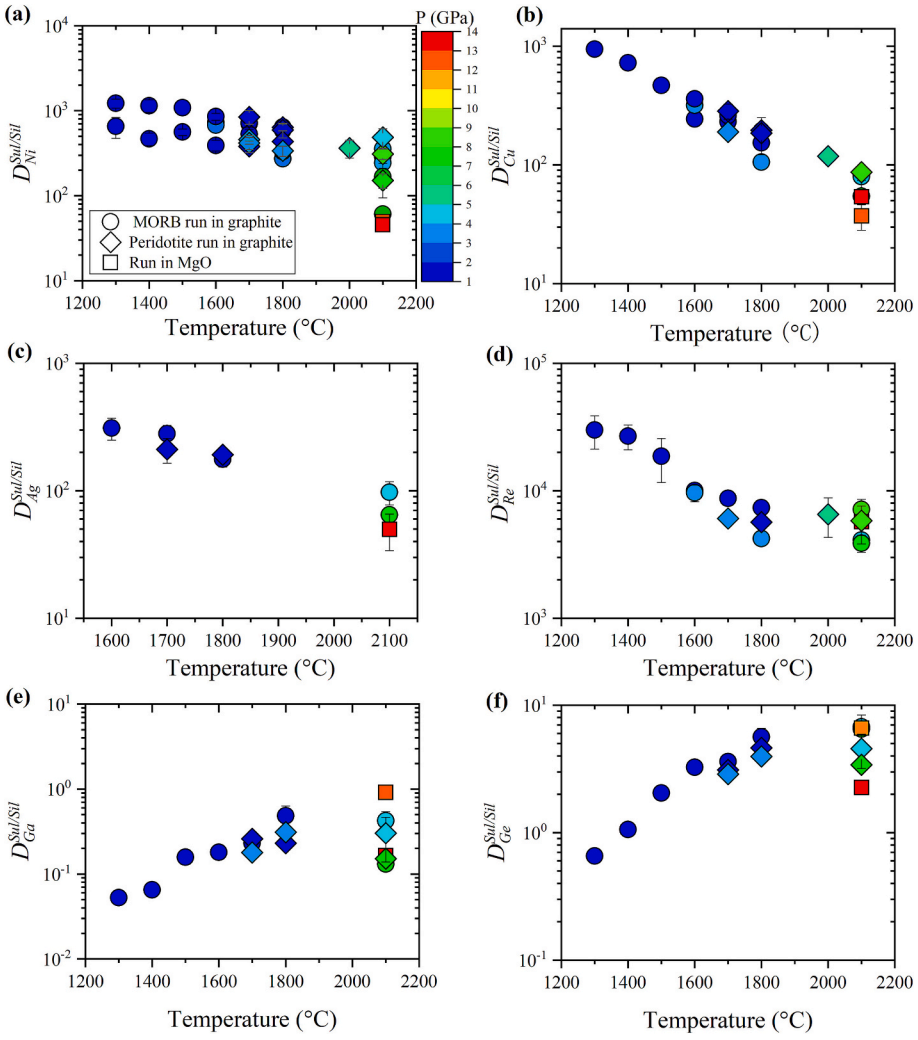

Fig. 4. Sulfide liquid–silicate melt partition coefficients of chalcophile and siderophile elements ($D_{CSE}^{Sul/Sil}$) as a function of temperature. The data are color-coded for pressure. Note that the $D_{CSE}^{Sul/Sil}$ for Ni, Cu, Ag, and Re decrease with increasing temperature, while the $D_{CSE}^{Sul/Sil}$ for Ga and Ge increase with increasing temperature.

(Blanchard et al., 2021; Laurenz et al., 2016; Righter et al., 2018; Righter et al., 2020; Rubie et al., 2016; Steenstra et al., 2022; ZhangZhou et al., 2024). Steenstra et al. (2022) suggested that sulfide liquid exsolution may not have occurred in the Earth's deep magma ocean based on a few SCSS values obtained directly relevant for a deep terrestrial magma ocean. However, most of these studies reached a consensus that sulfide liquid exsolution may have only occurred in the Earth's deep magma ocean (> 50 GPa) due to the pressure-suppressed SCSS, or in the shallow magma ocean (< 10 GPa) until sufficient silicate crystallization occurred to drive the S content of the silicate magma ocean to values higher than the corresponding SCSS. In this study, we employed the two most recent SCSS models (Blanchard et al., 2021; ZhangZhou et al., 2024) to investigate the exsolution of sulfide liquids in the Earth's final solidifying magma ocean. Fig. 9 illustrates that the exsolution of sulfide liquids occurs at ~75 GPa in the Earth's magma ocean if it has initial sulfur concentrations between 400 and 600 μg/g, which are the lower endmember values used in previous studies (Laurenz et al., 2016; Rubie et al., 2016; ZhangZhou et al., 2024). This finding is consistent with the conclusions of previous studies that emphasized the importance of mantle-to-core segregation of sulfide liquids occurring in the Earth's deep magma ocean (Laurenz et al., 2016; Righter et al., 2018; Righter et al., 2020; Rubie et al., 2016). Fig. 9 also indicates that a small quantity of sulfide liquids may also exsolve at pressures <30 GPa, contingent on the SCSS model employed. The mantle-to-core segregation of sulfide liquids occurring in a shallow magma ocean is well consistent with the findings of previous studies that emphasized the potential for the mantle-to-core segregation of sulfide liquids in a largely crystalline mantle (Ballhaus et al., 2017; Ballhaus et al., 2013; Kiseeva and Wood, 2015; Wood et al., 2008). The question of whether the exsolved sulfide liquids in a shallow magma ocean can be segregated into the core through the upper mantle percolation remains unresolved (Blanchard et al., 2021; Hart and Gaetani, 2016; Holzheid et al., 2000; Solomatov, 2015). In this study, we evaluate the effects of the mantle-to-core segregation of sulfide liquids on the CSE abundances of the silicate Earth, taking both scenarios into account.

In order to evaluate the effect of mantle-to-core segregation of sulfide liquids in the deep magma ocean, a series of conditions were employed. First, we employed a pressure of ~75 GPa for the exsolution of sulfide liquids in the magma ocean, with the corresponding temperature constrained by the peridotite liquidus (mean value derived from Andrault et al. (2011) and Fiquet et al. (2010)). Secondly, the mantle peridotite composition (Palme and O'Neill, 2014) was employed as the silicate magma ocean composition. The sulfide liquids were assumed to be Fe-Ni-Cu-S-O, with the Cu and Ni contents calculated using Eq. (1), and the O content calculated using the data provided by Kiseeva et al. (2015). Thirdly, the aforementioned Eq. (1), along with the specified pressure, temperature, and composition of the sulfide liquid and silicate melt, was employed to calculate $D_{CSE}^{Sul/Sil}$. Furthermore, it was assumed

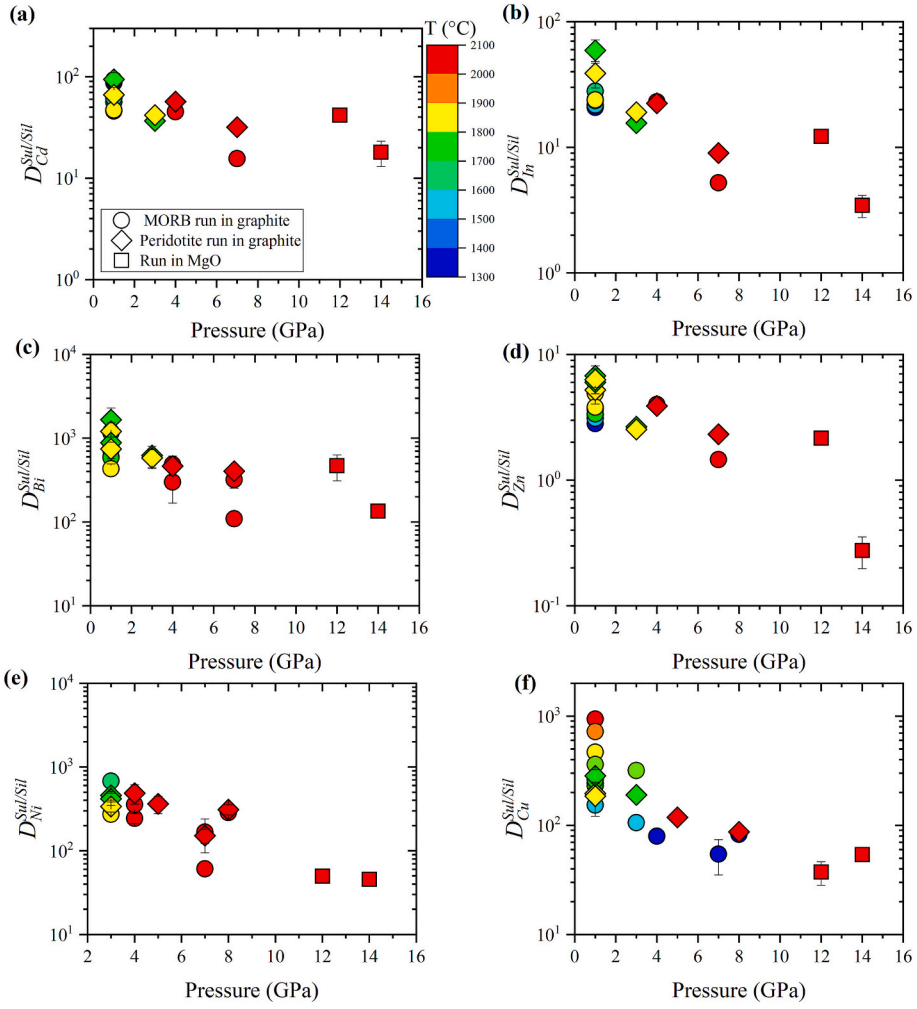

Fig. 5. Sulfide liquid–silicate melt partition coefficients of chalcophile and siderophile elements ($D_{CSE}^{Sul/Sil}$) as a function of pressure. The data are color-coded for temperature. Note that the $D_{CSE}^{Sul/Sil}$ for Cd, In, Bi, Zn, Ni and Cu decrease with increasing pressure.

that complete equilibrium had been reached between the segregated sulfide liquids and the silicate magma ocean.

Fig. 10a illustrates the calculated $D_{CSE}^{Sul/Sil}$ for a range of elements, including Ni, Co, Zn, Ga, Ge, Pb, Mo, In, Cd, Sb, Cu, Ag, Re, and Bi. These values are below 50, with the exception of Re, which is primarily due to the elevated pressure and temperature conditions at which the sulfide liquids exsolved. The calculated $D_{Re}^{Sul/Sil}$ values are ~1 × 10^5. Fig. 10b illustrates the modeled mantle CSE abundances (normalized by the observed present-day mantle CSE abundances) as a function of the mass of the segregated sulfide liquids. As illustrated in Fig. 10b, the concentrations of Zn, Ga, Ge, Pb, Mo, Co, In, Cd, Sb, Cu, Ag, Ni, and Bi in the silicate Earth exhibit a decrease of less than 10 % due to the mantle-to-core segregation of sulfide liquids with a mass as high as 1 % of the silicate Earth mass, which was the maximum mass proposed in previous studies (Laurenz et al., 2016; Righter et al., 2018; Rubie et al., 2016; Yoshizaki and McDonough, 2021). However, the abundance of Re in the silicate Earth can be significantly diminished as a consequence of the elevated $D_{Re}^{Sul/Sil}$. These findings illustrate that the mantle-to-core segregation of sulfide liquids in the deep magma ocean has a negligible impact on the abundances of Zn, Ga, Ge, Pb, Mo, Co, In, Cd, Sb, Cu, Ag, Ni and Bi in the silicate Earth. However, it can result in the sequestration of a significant portion of Re. In other words, only Re among these studied elements may serve as a sensitive indicator of the mantle-to-core segregation of sulfide liquids occurring in the deep magma ocean due to its highly chalcophile nature. Furthermore, the $D_{Cu,Pb}^{Sul/Sil}$ values (5 and 6, respectively) predicted at the conditions of the deep magma ocean (Fig. 10a) are considerably lower than those (100–500 and 40–50, respectively) required to explain the observed Cu and Pb isotopic compositions of the silicate Earth (Savage et al., 2015; Wood et al., 2008). Therefore, the mantle-to-core segregation of sulfide liquids in the deep magma ocean cannot explain the observed Cu and Pb isotopic compositions of the silicate Earth (Fig. S3).

Subsequently, the impact of the mantle-to-core segregation of sulfide liquids occurring in a shallow magma ocean on the CSE abundances of the silicate Earth was assessed. In this instance, a pressure of 10 GPa was employed, and the corresponding temperature was estimated to be ~2200 °C. Furthermore, it was assumed that all elements under consideration are highly incompatible in mantle minerals, and thus only present in the residual melt following crystallization. This may be the case for elements such as Cu and Ag with very low mineral–silicate melt partition coefficients (Li et al., 2022), but not the case for Co, Ni, Zn, As, Cd, In, Zn, Ge, and Ga. These elements are more concentrated in mantle silicate minerals (Bédard, 2007; Davis et al., 2013; Le Roux et al., 2011; Witt-Eickschen et al., 2009). Nevertheless, this would not affect our conclusions, which will be presented below. Fig. 11a depicts the calculated $D_{CSE}^{Sul/Sil}$, which are less than 50 for Ga, Zn, Co, Sb, Pb, In, Cd, Ge and Mo, between 80 and 90 for Cu and Ag, between 230 and 280 for Ni and Bi, and 11,500 for Re. Fig. 11b illustrates the modeled mantle CSE abundances (normalized by the observed present-day mantle CSE

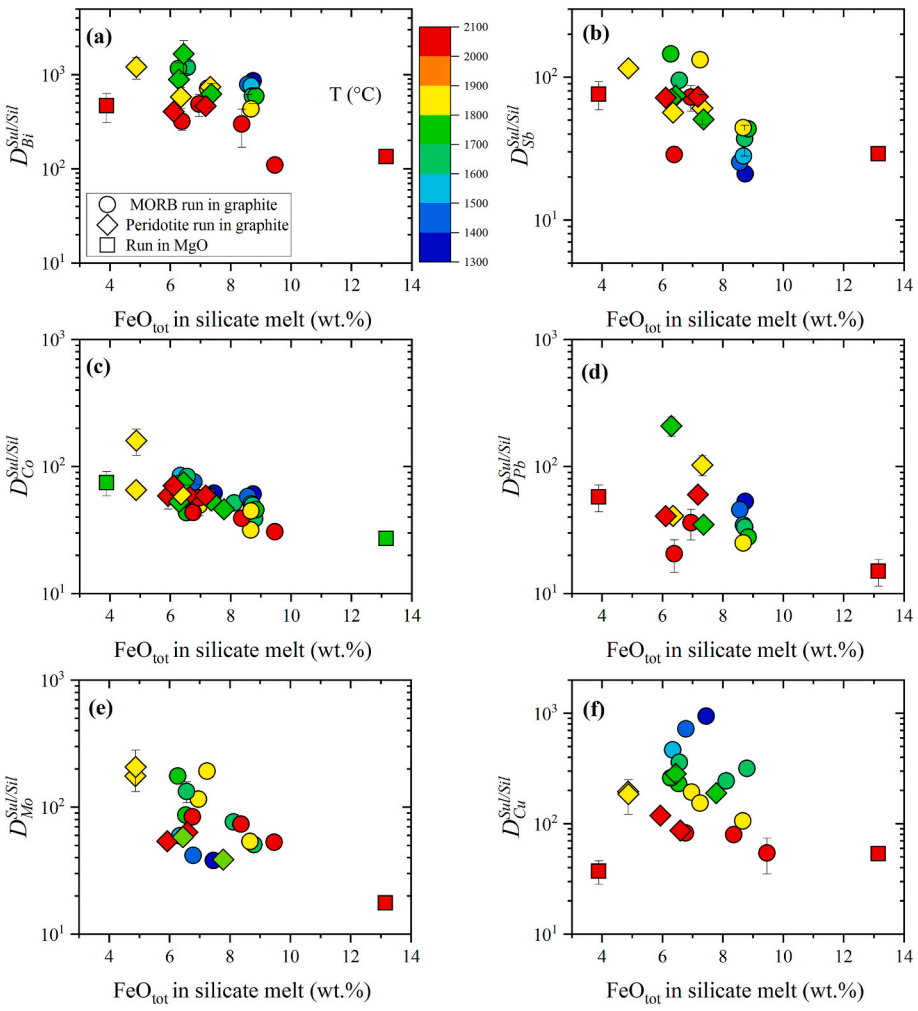

Fig. 6. Sulfide liquid–silicate melt partition coefficients of chalcophile and siderophile elements ($D_{CSE}^{Sul/Sil}$) as a function of FeO_{tot} contents of the silicate melts. The data are color-coded for temperature. Note that the $D_{CSE}^{Sul/Sil}$ for Sb, Bi, Co, Pb, Mo and Cu decrease with increasing FeO_{tot} contents of the silicate melts.

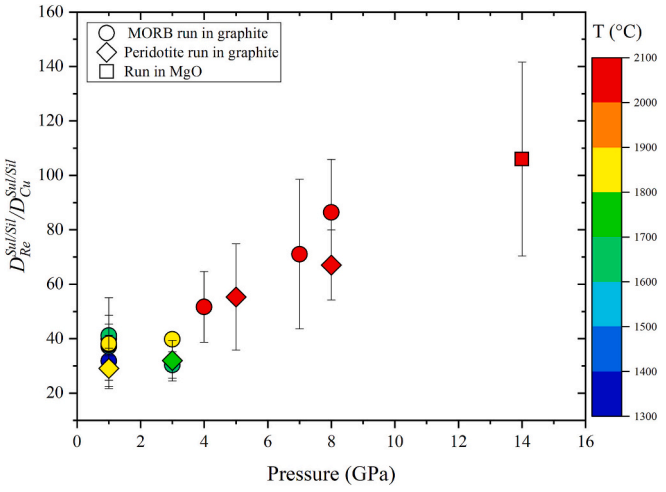

Fig. 7. The $D_{Re}^{Sul/Sil}$ / $D_{Cu}^{Sul/Sil}$ ratio as a function of pressure. The data are color-coded for temperature. Note that the $D_{Re}^{Sul/Sil}$ / $D_{Cu}^{Sul/Sil}$ ratio increases with increasing pressure.

abundances) as a function of the mass of the segregated sulfide liquids. In Fig. 11b, the used maximum mass of the segregated sulfide liquids is 0.07 % of the silicate Earth mass, which is equivalent to 1 % sulfide liquid relative to the mass of the shallow magma ocean at a depth of 10 GPa. As illustrated in Fig. 11b, the proportions of CSEs extracted by sulfide liquids from the silicate Earth exhibit variability: < 10 % for Ge, Ga, In, and Zn; 10–30 % for Cd, Pb, Sb, and Co; 50–70 % for Cu, Ag, Ni, and Bi; and nearly all the Re. The incorporation of CSEs in mantle minerals would result in a reduction in the proportions of CSEs extracted by sulfide liquids. To illustrate, the mantle Ni, Co, Ge, Ga, In, Zn, and Cd could be largely unaffected by mantle-to-core segregation of sulfide liquids if their incorporation in mantle minerals is taken into account, given the significant crystallization of the initial magma ocean at a magma ocean depth of 10 GPa. However, the proportions of Cu and Pb extracted by sulfide liquids are sufficiently high to explain the Cu and Pb isotopic compositions of the silicate Earth, as previously proposed by several models (Ballhaus et al., 2017; Hart and Gaetani, 2006; Savage et al., 2015; Wood et al., 2008).

4.3. The accretion of Re and the addition of a late veneer on Earth

As discussed above, Re is more sensitive to the mantle-to-core segregation of sulfide liquids in comparison to the other CSEs that were studied. The mantle-to-core segregation of sulfide liquids with a mass of 0.1 wt% of the silicate Earth would result in the extraction of

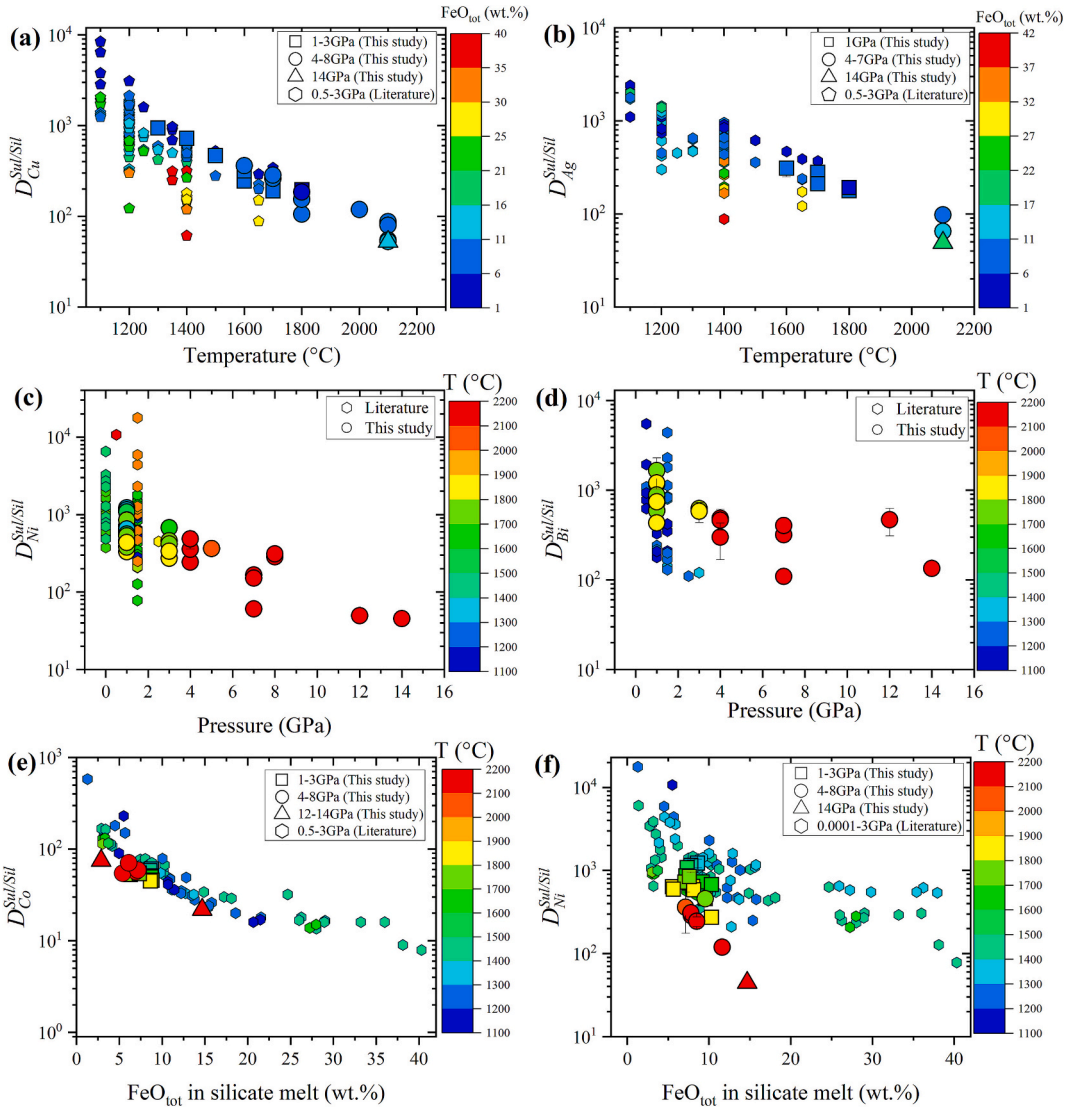

Fig. 8. Comparison of the presently obtained $D_{CSE}^{Sul/Sil}$ and previous data. The $D_{CSE}^{Sul/Sil}$ data were plotted as a function of temperature, pressure, or FeO$_{tot}$ content of the silicate melt. (a-b) The $D_{CSE}^{Sul/Sil}$ for Cu and Ag decrease with increasing temperature. The data are color-coded for FeO$_{tot}$ content of the silicate melt. (c-d) The $D_{CSE}^{Sul/Sil}$ for Ni and Bi decrease with increasing pressure. The data are color-coded for temperature. (e-f) The $D_{CSE}^{Sul/Sil}$ for Co and Ni decrease with increasing FeO$_{tot}$ content of the silicate melt. The data are color-coded for temperature. Literature data were taken from (Brenan, 2008, 2015; Gaetani and Grove, 1997; Kiseeva and Wood, 2013; Kiseeva and Wood, 2015; Li and Audétat, 2012; Li, 2014; Li and Audétat, 2015; Li et al., 2021; Peach and Mathez, 1993).

over 90 % of the Re present in the silicate Earth (Figs. 10b and 11b). The impact of mantle-to-core segregation of sulfide liquids on Re is analogous to that proposed for PGEs (Laurenz et al., 2016; Righter et al., 2018; Rubie et al., 2016). In order to gain a deeper understanding of the Earth's accretion of Re, we applied our $D_{Re}^{Sul/Sil}$ and the metal–silicate partition coefficients of Re ($D_{Re}^{Met/Sil}$) obtained in a previous study (Mann et al., 2012) to the accretion model of Rubie et al. (2016). Fig. 12 illustrates that the formation of Earth's core could have resulted in the concentration of Re in the silicate Earth reaching 1.1×10^{-4} to 7×10^{-5} ng/g, based on an initial Re content of either a CI-chondrite (38.1 ng/g) or an enstatite chondrite (63.9 ng/g) (Day et al., 2016; Fischer-Gödde et al., 2011; Horan et al., 2003). The subsequent mantle-to-core segregation of sulfide liquids could have resulted in an even lower mantle Re abundance, potentially reaching an extremely low value of less than 2×10^{-6} ng/g. This value is significantly lower than the observed present-day value of 0.32 ± 0.05 ng/g in the silicate Earth (Wang et al., 2018). Therefore, the addition of a late veneer with a mass of ~0.5 % of the Earth was required to elevate the Re abundance of the silicate Earth to its present-day value. Accordingly, the late veneer may have constituted a significant source of Re in the silicate Earth, as has been proposed for PGEs (Dale et al., 2012; Day et al., 2016; Laurenz et al., 2016; Righter et al., 2018; Rubie et al., 2016). The late veneer may have been differentiated (Marchi et al., 2017) or unprocessed chondritic materials (Albarede, 2009; Wang and Becker, 2013) and may have originated from the inner or outer solar system (Fischer-Godde and Kleine, 2017; Varas-Reus et al., 2019). These considerations should not alter the role of the late veneer in supplying Re and PGEs to the proto-Earth.

4.4. *Implications for the accretion of volatile CSEs on Earth*

Several models have been put forth to explain the accretion of volatile CSEs on Earth. (**I**) The initial model proposed that the Earth formed from homogeneous materials that were partially depleted of volatile elements (Righter et al., 2011; Righter et al., 2017). All volatile elements participated in the core–mantle partitioning that occurred in the magma ocean. The depletion of certain volatile CSEs, such as As, Sb, and Ge, can be attributed to their preferential partitioning into the core. However,

Table 8
Fitting coefficients obtained for Eq. (1)[¥].

	No. of data (n)	a	1σ	b	1σ	c	1σ	ε^{FeO}	1σ	ε^{NiS}	1σ	$\varepsilon^{CuS0.5}$	1σ	e ($logAl_2O_3$)	1σ	e (logCaO)	1σ	C	1σ	R^2	SD (1σ)
Zn	$n = 94$	−2061	252	−241	21	−1.26	0.07	−1.68	0.39	0.51	0.26	−1.16	0.16					2.94	0.18	0.87	0.14
Ga	$n = 45$	−4232	434	−85	23	−1.28	0.12	−3.36	0.58			−1.25	0.52					2.58	0.25	0.89	0.14
Ge	$n = 45$	−4015	429	−100	23	−0.96	0.08					−1.79	0.44					3.51	0.24	0.88	0.14
Pb	$n = 94$	449	185	−33	11	−1.07	0.04					−0.36	0.11					2.36	0.13	0.89	0.11
Co	$n = 94$	552	170	−31	14	−1	0.05	0.40	0.27	−0.57	0.18	0.36	0.11					2.40	0.12	0.92	0.09
In	$n = 64$	−695	259	−175	16	−0.98	0.07	0.52	0.32			−1.23	0.33					2.76	0.16	0.93	0.09
Cd	$n = 78$	2202	189	−43	14	−1.05	0.03			0.36	0.15	−0.36	0.10					1.57	0.12	0.95	0.08
Cu	$n = 145$	4326	189	−33	12	−0.26	0.07	2.63	0.35	0.72	0.24							0.51	0.13	0.91	0.13
Ag	$n = 91$	3436	236	−65	24	−0.24	0.07	2.14	0.38	0.73	0.25	−0.26	0.09					1.04	0.17	0.89	0.13
Ni	$n = 119$	2161	293	−102	19	−0.76	0.06	0.65	0.23	−0.47	0.10	0.36	0.34					2.45	0.18	0.88	0.12
Bi	$n = 22$	2553	365	−50	23	−0.76	0.16											2.26	0.3	0.89	0.32
Mo	$n = 26$	−3295	525	−103	31	−1.37	0.35			−6.33	2.17			−1.21	0.46	1.87	0.55	5.30	0.38	0.86	0.36
Sb	$n = 64$	−2439	286	−83	17	−1.13	0.04			−1.85	0.19	−2.18	0.32					3.98	0.17	0.93	0.21
Re	$n = 19$	4836	331	114	22	−1.22	0.24											2.47	0.23	0.89	0.37

1σ is the standard deviation of each coeffient reported.
R^2 is the correlation coefficient, which provides a measure of how well the observed results are reproduced by the equation.

$$logD_{CSE}^{Sul/Sil} = C + \frac{a}{T} + b\frac{P}{T} + c\cdot log\left[X_{FeO_{1bt}}^{Sil}\right]_{corr} + d \bullet \Delta FMQ + 1673/T\cdot\left[\varepsilon_{CSE}^{FeO}\cdot log\left(1 - x_{FeO}^{Sil}\right) + \varepsilon_{CSE}^{NiS}\cdot log\left(1 - x_{NiS}^{Sil}\right) + \varepsilon_{CSE}^{CuS_{0.5}}\cdot log\left(1 - x_{CuS_{0.5}}^{Sil}\right)\right] + \sum e_i\cdot logx_i^{Sil.}$$

this core–mantle partitioning model is unable to account for the disparate depletion patterns observed in many other volatile CSEs, including S, Pb, Cd, and Sn, as well as the non-depletion of In (Ballhaus et al., 2017; Wang et al., 2016). (**II**) A second model posits that the volatile CSEs of the silicate Earth may have been added during very late accretions, by the late veneer (Albarede, 2009), for example, when the metallic melt segregation to the core had become largely inactive (Ballhaus et al., 2017; O'Neill, 1991). Mantle-to-core segregation of sulfide liquids in a largely crystalline mantle was proposed as the mechanism responsible for the depletion of volatile CSEs in the silicate Earth (Ballhaus et al., 2017; Ballhaus et al., 2013; O'Neill, 1991). (**III**) A third and intermediate model proposed that the Earth formed by the accretion of volatile-poor materials, followed by a late accretion of 10–15 % of volatile-rich materials, such as CI chondrite-like materials (Braukmüller et al., 2019; Marty, 2012; Schönbächler et al., 2010). This model can explain the Ag isotopic composition and the "hockey stick" pattern of volatile lithophile elements of the silicate Earth (Braukmüller et al., 2019; Righter et al., 2020; Schönbächler et al., 2010). The experimental studies, which focused on the metal–silicate partitioning of Cd, Bi, Sb, Tl, and S (Kubik et al., 2021a; Suer et al., 2017) and the metal–silicate isotope fractionation of Sn (Kubik et al., 2021b), showed that the depletion of these elements and the Sn isotopic composition of the silicate Earth can be explained only when volatile CSEs were added during the Earth's last 10–20 % accretion. However, experimental studies have also indicated that the late accretion of volatile-rich materials to the Earth may result in the overabundance of certain volatile CSEs, such as Bi, Ag, and Cu, in the silicate Earth after the cessation of core formation, which necessitates the mantle-to-core segregation of sulfide liquids in a deep magma ocean to reduce the volatile CSE abundances (Righter et al., 2018, 2020). (**IV**) An additional model that can account for the depletion pattern of volatile CSEs in the silicate Earth is partial melting and vaporization on the Earth's precursor bodies (Norris and Wood, 2017). Similar melting and vaporization models have also been proposed to explain the S, Se, Te, Mg, and Si isotope compositions of the silicate Earth (Hin et al., 2017; Li, 2021; Lu et al., 2024; Wang et al., 2021; Wang et al., 2023; Young et al., 2019). Nevertheless, based on elemental ratios and stable isotopes (Campbell and O'Neill, 2012; O'Neill and Palme, 2008; Pringle and Moynier, 2017; Siebert et al., 2018), it has been argued that post-nebular volatile loss was restricted on the Earth and may have not played a major role in determining the depletion of volatile CSEs in the silicate Earth (Braukmüller et al., 2019; Wang et al., 2016).

The results of our modeling allow us to test some of the aforementioned models. The results of our modeling demonstrate that mantle-to-core segregation of sulfide liquids in a deep magma ocean has a negligible impact on the abundances of volatile CSEs in the silicate Earth. Furthermore, our findings indicate that mantle-to-core segregation of sulfide liquids in a shallow magma ocean is insufficient to extract more than 75 % of the volatile CSEs present in the silicate Earth. Our modeling results suggest that volatile CSEs in the silicate Earth cannot have been as depleted as those observed presently (Fig. 13) if volatile CSEs were delivered after the Earth's core formation had been inactive, as proposed by (Ballhaus et al., 2017; 2013; O'Neill, 1991). Fig. 13 illustrates that the observed depletion pattern of Bi, Sb, As, Ge, Ag, and Cu in the silicate Earth is inconsistent with mantle-to-core segregation of sulfide liquids at *P–T* conditions corresponding to a deep or shallow magma ocean. Fig. 13 also illustrates that, in order to explain the depletion pattern of volatile CSEs in the silicate Earth by using the mantle-to-core segregation of sulfide liquids alone, the order of the $D_{CSE}^{Sul/Sil}$ values is as follows: $D_{As}^{Sul/Sil} > D_{Sb}^{Sul/Sil} \approx D_{Ag}^{Sul/Sil} \approx D_{Ge}^{Sul/Sil} > D_{Sb}^{Sul/Sil} > D_{Bi}^{Sul/Sil} > D_{Cu}^{Sul/Sil} > D_{Cd}^{Sul/Sil} > D_{Pb}^{Sul/Sil} \approx D_{Sn}^{Sul/Sil} > D_{Ga}^{Sul/Sil}$. However, this order in $D_{CSE}^{Sul/Sil}$ is markedly disparate from our experimental results and the predicted $D_{CSE}^{Sul/Sil}$ values at the magma ocean conditions (Figs. 10a and 11a). In light of these considerations, we propose that the model proposed by (Ballhaus et al., 2017;

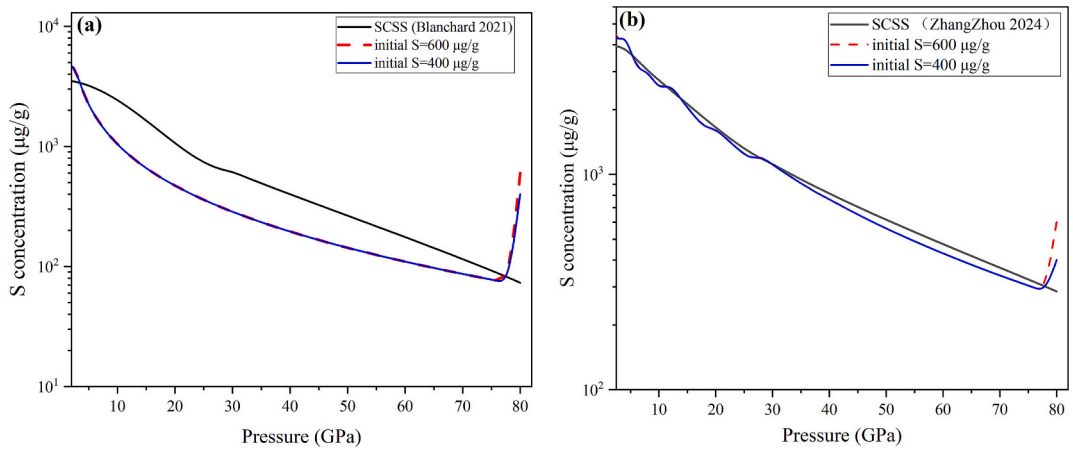

Fig. 9. The evolution of the SCSS and S content in the silicate magma ocean during Earth's final solidification. The composition of the primitive mantle (Palme and O'Neill, 2014) and the peridotite liquidus temperature were used to calculate the SCSS values using the models of Blanchard et al. (2021) and ZhangZhou et al. (2024). In addition, 400–600 μg/g of S was assumed in the magma ocean before solidification, and S was assumed to be perfectly incompatible in silicate minerals during the solidification.

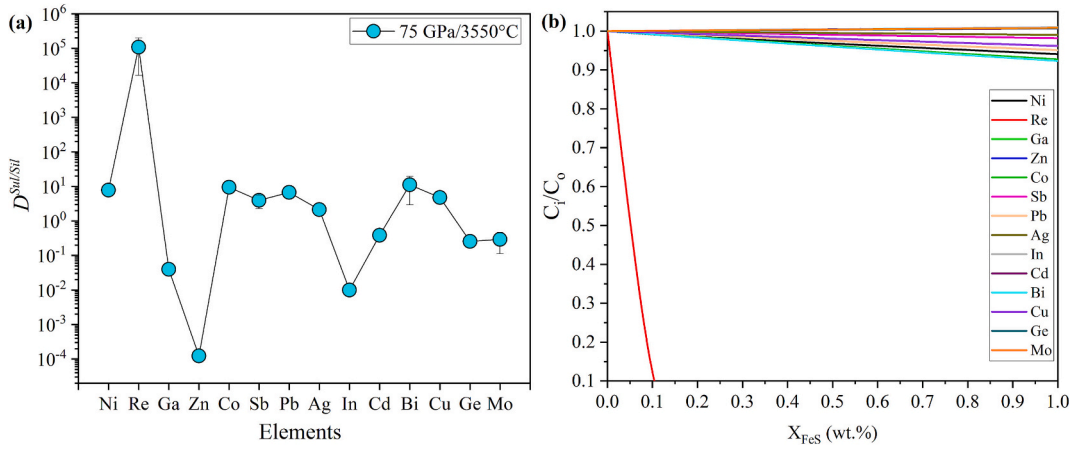

Fig. 10. The effect of mantle-to-core segregation of sulfide liquids in a deep magma ocean on the abundances of siderophile and chalcophile elements (CSEs) in the silicate Earth. (a) The $D_{CSE}^{Sul/Sil}$ were calculated for a deep magma ocean at 75 GPa and 3550 °C using Eq. (1). The error bars were based on 1-sigma standard deviation for $D_{CSE}^{Sul/Sil}$ (Table 8). (b) Modeled mantle CSE abundances (C_i), normalized by the observed present-day mantle CSE abundances (C_o), as a function of the mass of segregated sulfide liquids (X_{FeS}, wt%) in the deep magma ocean. The mass of segregated sulfide liquids (X_{FeS}, wt%) is relative to the mass of the silicate Earth. The uncertainties of C_i/C_o are ≤30 % based on the errors of $D_{CSE}^{Sul/Sil}$.

2013; O'Neill, 1991), which assumed the accretion of Earth's volatile CSEs following the cessation of core formation and employed the mantle-to-core segregation of sulfide liquids to elucidate the depletion pattern of volatile CSEs in the silicate Earth, may not be a viable explanation.

Our modeling results are also inconsistent with the model proposal by (Righter et al., 2018; Righter et al., 2020), which emphasized the importance of the mantle-to-core segregation of sulfide liquids in a deep magma ocean in removing the over-abundant Ag and Bi in the silicate Earth after the cessation of core formation. Righter et al. (2020) employed a $D_{Bi}^{Sul/Sil}$ value of 500 and a $D_{Ag}^{Sul/Sil}$ value of 2000, derived from the experimental outcomes obtained at crust–mantle conditions (Kiseeva and Wood, 2015; Li and Audétat, 2012). These values are significantly higher than those utilized in the present study (Fig. 10a). It can thus be concluded that any over-abundant Ag and Bi in the silicate Earth after the cessation of core formation cannot have been removed by the mantle-to-core segregation of sulfide liquids occurring in the deep magma ocean. The issue of the overabundance of Ag and Bi could be resolved if the Earth formed from less volatile-rich materials; however, this would require an alternative explanation for the Ag isotopic composition of the silicate Earth (Righter et al., 2020).

The above discussion illustrates that if the Earth acquired its volatile CSEs subsequent to the cessation of core formation, the segregation of sulfide liquids alone cannot account for the depletion pattern of volatile CSEs in the silicate Earth, irrespective of whether the sulfide liquids were segregated from a deep magma ocean or a largely crystalline magma ocean. The accretion of Earth's volatile CSEs during the main accretion phase, or during the last 10–20 % of accretion, is consistent with recent findings that the Earth's highly volatile elements (hydrogen, carbon, and nitrogen) were primarily delivered during the main accretion phase and participated in the core formation process (Broadley et al., 2022; Grewal et al., 2019; Li et al., 2016; Marty, 2012; Shi et al., 2022). However, if we accept that the Earth acquired its volatile CSEs during the main accretion phase or during the last 10–20 % of accretion, future research should concentrate on the circumstances under which the partitioning of volatile CSEs into the core can elucidate the general depletion pattern of volatile CSEs and their isotopic compositions in the silicate Earth, with or without invoking the mantle-to-core segregation of sulfide liquids.

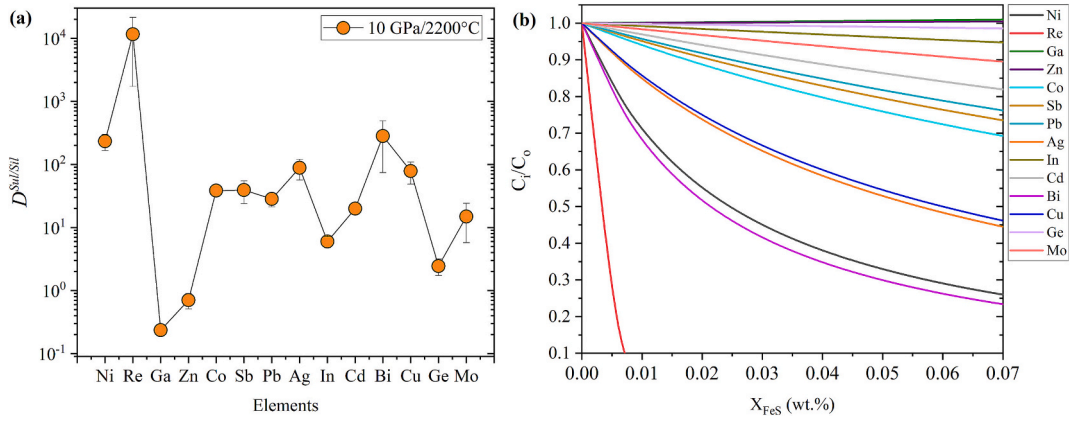

Fig. 11. The effect of mantle-to-core segregation of sulfide liquids in a shallow magma ocean on the abundances of siderophile and chalcophile elements (CSEs) in the silicate Earth. (a) The $D_{CSE}^{Sul/Sil}$ were calculated for a shallow magma ocean at 10 GPa and 2200 °C using Eq. (1). The error bars were based on 1-sigma standard deviation for $D_{CSE}^{Sul/Sil}$ (Table 8). (b) Modeled mantle CSE abundances (C_i), normalized by the observed present-day mantle CSE abundances (C_o), as a function of the mass of segregated sulfide liquids (X_{FeS}, wt%) in the shallow magma ocean. The mass of segregated sulfide liquids (X_{FeS}, wt%) is relative to the mass of the silicate Earth. The uncertainties of C_i/C_o are ≤30 % based on the errors of $D_{CSE}^{Sul/Sil}$.

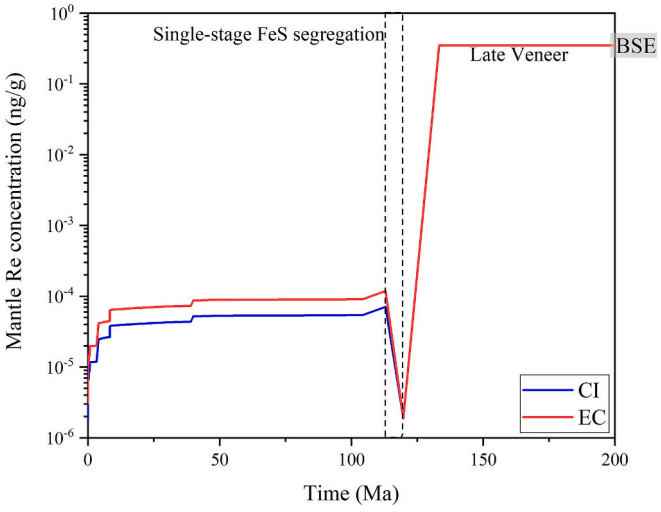

Fig. 12. The evolution of the Re concentration in the silicate Earth with the accretion time using an initial CI chondrite or enstatite chondrite (EC) composition. The results show that core formation and a late single-stage sulfide liquid segregation at 113 My result in significantly low Re concentration, and the addition of a late veneer is required to achieve the observed present-day Re abundance in the bulk silicate Earth (BSE). The observed Re content in the BSE was taken from Wang et al. (2018). The Earth's accretion model was adopted from Rubie et al. (2016).

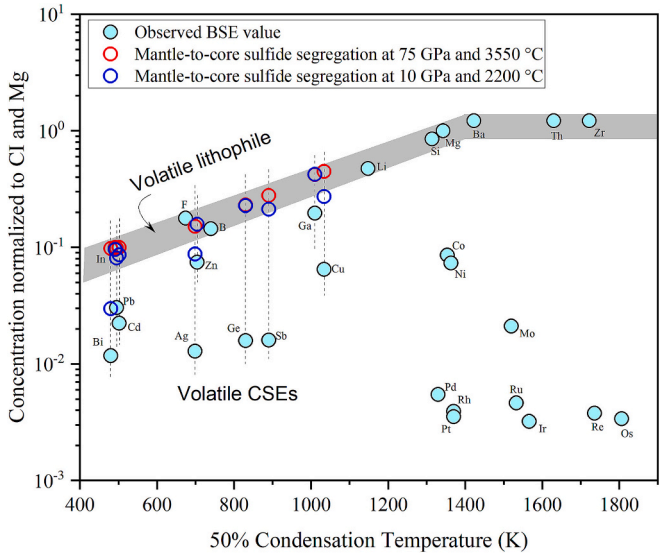

Fig. 13. Abundances of elements in the bulk silicate Earth (BSE) relative to CI chondrites (Palme and O'Neill, 2014) and Mg = 1.0 plotted as a function of 50 % condensation temperature (Wood et al., 2019) from a gas of solar composition. The results showed that the segregation of 0.07 wt% sulfide liquids (shallow magma ocean) or 1 wt% sulfide liquid (deep magma ocean) cannot explain the observed contents of volatile siderophile and chalcophile elements (CSEs) in the BSE. Note that the mass of segregated sulfide liquids (X_{FeS}, wt%) is relative to the mass of the silicate Earth.

5. Conclusions

We have experimentally determined $D_{CSE}^{Sul/Sil}$ at 1300–2100 °C and 1–14 GPa for Co, Ni, Cu, Zn, Ga, Ge, Mo, Ag, Cd, In, Sb, Re, Pb and Bi. The $D_{CSE}^{Sul/Sil}$ were parameterized as a multi-function of pressure, temperature, and composition of the silicate melt and sulfide liquid. We used this parameterization to predict the $D_{CSE}^{Sul/Sil}$ during the mantle-to-core segregation of sulfide liquids that occurred in the Earth's solidifying magma ocean, and to understand the role of the Hadean matte in determining the CSE abundances of the silicate Earth. We show that the mantle-to-core segregation of sulfide liquids occurring in the deep magma ocean at 75 GPa has a negligible role in influencing the CSE abundances (except for Re) and the Cu, Ag, and Pb isotopic compositions of the silicate Earth. Mantle-to-core segregation of sulfide liquids in a shallow magma ocean at 10 GPa can extract 10–70 % of the Pb, Cu, Ag, and Bi in the silicate Earth, and explain the Cu and Pb isotopic compositions of the silicate Earth. However, the depletion pattern of volatile CSEs in the silicate Earth cannot be explained by the mantle-to-core segregation of sulfide liquids if the Earth's volatile CSEs were delivered very late, when the metal segregation into the core remained largely inactive. This is independent of whether the mantle-to-core segregation of sulfide liquids occurred in a deep or shallow magma ocean. With respect to Re, the formation of the Earth's core and the subsequent mantle-to-core segregation of sulfide liquids could have significantly depleted the silicate Earth in Re, and the addition of a late veneer should have followed to explain the observed present-day Re abundance of the silicate Earth. Previous models that have used mantle-to-core segregation of sulfide liquids as an important approach to

explain the depletion of volatile CSEs in the silicate Earth need to be re-examined. Finally, we like to point out that the extrapolation of our $D_{CSE}^{Sul/Sil}$ parameterization to the Earth's deep magma ocean necessitates future experiments at significantly higher *P*–*T* conditions.

CRediT authorship contribution statement

M. Zhang performed the experiments and analyses. Y. Li concieved and supervised the study. Y. Li and M. Zhang interpreted the data and wrote the paper.

Declaration of competing interest

The authors declare that they have no known competing financial interests or personal relationships that could have appeared to influence the work reported in this paper.

Acknowledgments

M. Zhang thanks W. Wang for performing some experiments and analyses reported in this study. Fangyue Wang is appreciated for his help with LA–ICP–MS analyses. We also thank Claudia Romano for the handling of this paper and two anonymous reviewers for their constructive comments.

Appendix A. Supplementary data

Supplementary data to this article can be found online at https://doi.org/10.1016/j.chemgeo.2025.122671.

Data availability

All data are included in the paper and the Supplementary Material.

References

Albarede, F., 2009. Volatile accretion history of the terrestrial planets and dynamic implications. Nature 461 (7268), 1227–1233.
Andrault, D., et al., 2011. Solidus and liquidus profiles of chondritic mantle: implication for melting of the Earth across its history. Earth Planet. Sci. Lett. 304 (1–2), 251–259.
Ballhaus, C., Sylvester, P., 2000. Noble metal enrichment processes in the Merensky Reef, Bushveld complex. J. Petrol. 41 (4), 545–561.
Ballhaus, C., Bockrath, C., Wohlgemuth-Ueberwasser, C., Laurenz, V., Berndt, J., 2006. Fractionation of the noble metals by physical processes. Contrib. Mineral. Petrol. 152 (6), 667–684.
Ballhaus, C., et al., 2013. The U/Pb ratio of the Earth's mantle—a signature of late volatile addition. Earth Planet. Sci. Lett. 362, 237–245.
Ballhaus, C., et al., 2017. The great sulfur depletion of Earth's mantle is not a signature of mantle–core equilibration. Contrib. Mineral. Petrol. 172 (8).
Bédard, J.H., 2007. Trace element partitioning coefficients between silicate melts and orthopyroxene: parameterizations of D variations. Chem. Geol. 244 (1–2), 263–303.
Blanchard, I., Abeykoon, S., Frost, D.J., Rubie, D.C., 2021. Sulfur content at sulfide saturation of peridotitic melt at upper mantle conditions. Am. Mineral. 106 (11), 1835–1843.
Bockrath, C., Ballhaus, C., Holzheid, A., 2004. Fractionation of the platinum-group elements during mantle melting. Science 305 (5692), 1951–1953.
Bohlen, S.R., Montana, A., Kerrick, D.M., 1991. Precise determinations of the equilibria kyanite ⇌ sillimanite and kyanite ⇌ andalusite and a revised triple point for Al2SiO5 polymorphs. Am. Mineral. 76 (3–4), 677–680.
Bose, K., Ganguly, J., 1995. Quartz-coesite transition revisited: reversed experimental determination at 500–1200 °C and retrieved thermochemical properties. Am. Mineral. 80 (3–4), 231–238.
Botcharnikov, R.E., et al., 2013. Behavior of gold in a magma at sulfide-sulfate transition: revisited. Am. Mineral. 98 (8–9), 1459–1464.
Braukmüller, N., Wombacher, F., Funk, C., Münker, C., 2019. Earth's volatile element depletion pattern inherited from a carbonaceous chondrite-like source. Nat. Geosci. 12, 564–568.
Brenan, J.M., 2008. Re–Os fractionation by sulfide melt–silicate melt partitioning: a new spin. Chem. Geol. 248 (3–4), 140–165.
Brenan, J.M., 2015. Se–Te fractionation by sulfide–silicate melt partitioning: implications for the composition of mantle-derived magmas and their melting residues. Earth Planet. Sci. Lett. 422, 45–57.
Brenan, J.M., Bennett, N.R., Zajacz, Z., 2015. Experimental results on fractionation of the highly siderophile elements (HSE) at variable pressures and temperatures during planetary and magmatic differentiation. Rev. Mineral. Geochem. 81 (1), 1–87.
Broadley, M.W., Bekaert, D.V., Piani, L., Furi, E., Marty, B., 2022. Origin of life-forming volatile elements in the inner Solar System. Nature 611 (7935), 245–255.
Campbell, I.H., O'Neill, H.S.C., 2012. Evidence against a chondritic Earth. Nature 483 (7391), 553–558.
Chang, J., Audétat, A., 2018. Petrogenesis and metal content of Hornblende-Rich Xenoliths from two laramide-age magma systems in Southwestern USA: insights into the metal budget of Arc Magmas. J. Petrol. 59 (10), 1869–1898.
Dale, C.W., et al., 2012. Late accretion on the earliest planetesimals revealed by the highly siderophile elements. Science 336 (6077), 72–75.
Davis, F.A., Humayun, M., Hirschmann, M.M., Cooper, R.S., 2013. Experimentally determined mineral/melt partitioning of first-row transition elements (FRTE) during partial melting of peridotite at 3GPa. Geochim. Cosmochim. Acta 104, 232–260.
Day, J.M.D., Brandon, A.D., Walker, R.J., 2016. Highly Siderophile elements in Earth, Mars, the Moon, and Asteroids. Rev. Mineral. Geochem. 81 (1), 161–238.
Ding, S., Dasgupta, R., Tsuno, K., 2014. Sulfur concentration of martian basalts at sulfide saturation at high pressures and temperatures – implications for deep sulfur cycle on Mars. Geochim. Cosmochim. Acta 131, 227–246.
Feng, L., Li, Y., 2019. Comparative partitioning of Re and Mo between sulfide phases and silicate melt and implications for the behavior of Re during magmatic processes. Earth Planet. Sci. Lett. 517, 14–25.
Fiquet, G., et al., 2010. Melting of peridotite to 140 gigapascals. Science 329 (5998), 1516–1518.
Fischer-Godde, M., Kleine, T., 2017. Ruthenium isotopic evidence for an inner Solar System origin of the late veneer. Nature 541 (7638), 525–527.
Fischer-Gödde, M., Becker, H., Wombacher, F., 2011. Rhodium, gold and other highly siderophile elements in orogenic peridotites and peridotite xenoliths. Chem. Geol. 280 (3–4), 365–383.
Gaetani, G.A., Grove, T.L., 1997. Partitioning of moderately siderophile elements among olivine, silicate melt, and sulfide melt: constraints on core formation in the Earth and Mars. Geochim. Cosmochim. Acta 61 (9), 1829–1846.
Grewal, D.S., Dasgupta, R., Sun, C., Tsuno, K., Costin, G., 2019. Delivery of carbon, nitrogen, and sulfur to the silicate Earth by a giant impact. Sci. Adv. 5 (1), eaau3669.
Hart, S.R., Gaetani, G.A., 2006. Mantle Pb paradoxes: the sulfide solution. Contrib. Mineral. Petrol. 152 (3), 295–308.
Hart, S.R., Gaetani, G.A., 2016. Experimental determination of Pb partitioning between sulfide melt and basalt melt as a function of P, T and X. Geochim. Cosmochim. Acta 185, 9–20.
Hin, R.C., et al., 2017. Magnesium isotope evidence that accretional vapour loss shapes planetary compositions. Nature 549 (7673), 511–515.
Holzheid, A., Schmitz, M.D., Grove, T.L., 2000. Textural equilibria of iron sulfide liquids in partly molten silicate aggregates and their relevance to core formation scenarios. J. Geophys. Res. Solid Earth 105 (B6), 13555–13567.
Horan, M.F., Walker, R.J., Morgan, J.W., Grossman, J.N., Rubin, A.E., 2003. Highly siderophile elements in chondrites. Chem. Geol. 196 (1–4), 27–42.
Jenner, F.E., 2017. Cumulate causes for the low contents of sulfide-loving elements in the continental crust. Nat. Geosci. 10, 524–529.
Jenner, F.E., O'Neill, H.S.C., Arculus, R.J., Mavrogenes, J.A., 2010. The Magnetite Crisis in the Evolution of Arc-related Magmas and the initial Concentration of Au, Ag and Cu. J. Petrol. 51 (12), 2445–2464.
Kiseeva, E.S., Wood, B.J., 2013. A simple model for chalcophile element partitioning between sulphide and silicate liquids with geochemical applications. Earth Planet. Sci. Lett. 383, 68–81.
Kiseeva, E.S., Wood, B.J., 2015. The effects of composition and temperature on chalcophile and lithophile element partitioning into magmatic sulphides. Earth Planet. Sci. Lett. 424, 280–294.
Kiseeva, E.S., Fonseca, R.O.C., Smythe, D.J., 2017. Chalcophile elements and Sulfides in the Upper Mantle. Elements 13 (2), 111–116.
Kubik, E., et al., 2021a. Earth's volatile accretion as told by Cd, Bi, Sb and Tl core–mantle distribution. Geochim. Cosmochim. Acta 306, 263–280.
Kubik, E., et al., 2021b. Tracing Earth's volatile delivery with Tin. J. Geophys. Res. Solid Earth 126 (10).
Labidi, J., Cartigny, P., Moreira, M., 2013. Non-chondritic Sulphur isotope composition of the terrestrial mantle. Nature 501 (7466), 208–211.
Laurenz, V., Rubie, D.C., Frost, D.J., Vogel, A.K., 2016. The importance of sulfur for the behavior of highly-siderophile elements during Earth's differentiation. Geochim. Cosmochim. Acta 194, 123–138.
Le Roux, V., Dasgupta, R., Lee, C.T.A., 2011. Mineralogical heterogeneities in the Earth's mantle: constraints from Mn, Co, Ni and Zn partitioning during partial melting. Earth Planet. Sci. Lett. 307 (3–4), 395–408.
Lee, C.T., et al., 2012. Copper systematics in arc magmas and implications for crust-mantle differentiation. Science 336 (6077), 64–68.
Li, Y., 2014. Chalcophile element partitioning between sulfide phases and hydrous mantle melt: applications to mantle melting and the formation of ore deposits. J. Asian Earth Sci. 94, 77–93.
Li, Y., 2021. Sulfur evaporation in planetesimals. Nat. Geosci. 14, 803–805.
Li, Y., Audétat, A., 2012. Partitioning of V, Mn, Co, Ni, Cu, Zn, As, Mo, Ag, Sn, Sb, W, Au, Pb, and Bi between sulfide phases and hydrous basanite melt at upper mantle conditions. Earth Planet. Sci. Lett. 355-356, 327–340.
Li, Y., Audétat, A., 2013. Gold solubility and partitioning between sulfide liquid, monosulfide solid solution and hydrous mantle melts: implications for the formation of Au-rich magmas and crust–mantle differentiation. Geochim. Cosmochim. Acta 118, 247–262.

Li, Y., Audétat, A., 2015. Effects of temperature, silicate melt composition, and oxygen fugacity on the partitioning of V, Mn, Co, Ni, Cu, Zn, As, Mo, Ag, Sn, Sb, W, Au, Pb, and Bi between sulfide phases and silicate melt. Geochim. Cosmochim. Acta 162, 25–45.
Li, Y., Dasgupta, R., Tsuno, K., Monteleone, B., Shimizu, N., 2016. Carbon and sulfur budget of the silicate Earth explained by accretion of differentiated planetary embryos. Nat. Geosci. 9, 781–785.
Li, Y., et al., 2019. An essential role for sulfur in sulfide-silicate melt partitioning of gold and magmatic gold transport at subduction settings. Earth Planet. Sci. Lett. 528.
Li, Y., Audétat, A., Liu, Z., Wang, F., 2021. Chalcophile element partitioning between Cu-rich sulfide phases and silicate melt and implications for the formation of Earth's continental crust. Geochim. Cosmochim. Acta 302, 61–82.
Li, Y., Li, Y.-X., Xu, Z., 2022. The partitioning of Cu and Ag between minerals and silicate melts during partial melting of planetary silicate mantles. Geochim. Cosmochim. Acta 324, 280–311.
Liu, Z., Li, Y., 2023. Experimental constraints on the behavior of Pt and Re in oxidized arc magmas. Earth Planet. Sci. Lett. 603.
Liu, Y., et al., 2008. In situ analysis of major and trace elements of anhydrous minerals by LA-ICP-MS without applying an internal standard. Chem. Geol. 257 (1–2), 34–43.
Liu, X., et al., 2018. Aqueous fluid connectivity in subducting Oceanic Crust at the Mantle transition zone conditions. J. Geophys. Res. Solid Earth 123 (8), 6562–6573.
Lu, W., Weber, R., Zhang, Z., Li, Y., 2024. Experimental determination of Si, Mg, and Ca isotope fractionation during enstatite melt evaporation. Am. Mineral. 109 (7)., 1193–1202.
Mann, U., Frost, D.J., Rubie, D.C., Becker, H., Audétat, A., 2012. Partitioning of Ru, Rh, Pd, Re, Ir and Pt between liquid metal and silicate at high pressures and high temperatures - implications for the origin of highly siderophile element concentrations in the Earth's mantle. Geochim. Cosmochim. Acta 84, 593–613.
Marchi, S., Canup, R.M., Walker, R.J., 2017. Heterogeneous delivery of silicate and metal to the Earth by large planetesimals. Nat. Geosci. 11, 77–81.
Marty, B., 2012. The origins and concentrations of water, carbon, nitrogen and noble gases on Earth. Earth Planet. Sci. Lett. 313-314, 56–66.
Mavrogenes, J.A., O'Neill, H.S.C., 1999. The relative effects of pressure, temperature and oxygen fugacity on the solubility of sulfide in mafic magmas. Geochim. Cosmochim. Acta 63 (7–8), 1173–1180.
McDonough, W.F., Sun, S.-S., 1995. The composition of the Earth. Chem. Geol. 120 (3–4), 223–253.
Mungall, J.E., Brenan, J.M., 2014. Partitioning of platinum-group elements and au between sulfide liquid and basalt and the origins of mantle-crust fractionation of the chalcophile elements. Geochim. Cosmochim. Acta 125, 265–289.
Norris, C.A., Wood, B.J., 2017. Earth's volatile contents established by melting and vaporization. Nature 549 (7673), 507–510.
O'Neill, H.C., 1991. The origin of the Moon and the early history of the Earth-A chemical model. Part 2: the earth. Geochim. Cosmochim. Acta 55, 1159–1172.
O'Neill, H.S.C., Palme, H., 2008. Collisional erosion and the non-chondritic composition of the terrestrial planets. Trans. Royal Soc. A Math. Phys. Eng. Sci. 366, 4205–4238.
Palme, H., O'Neill, H.S.C., 2014. 3.1 - Cosmochemical estimates of Mantle Composition. In: Holland, H.D., Turekian, K.K. (Eds.), Treatise on Geochemistry (Second Edition). Elsevier, Oxford, pp. 1–39.
Peach, C., Mathez, E., 1993. Sulfide melt-silicate melt distribution coefficients for nickel and iron and implications for the distribution of other chalcophile elements. Geochim. Cosmochim. Acta 57 (13), 3013–3021.
Pringle, E.A., Moynier, F., 2017. Rubidium isotopic composition of the Earth, meteorites, and the Moon: evidence for the origin of volatile loss during planetary accretion. Earth Planet. Sci. Lett. 473, 62–70.
Righter, K., King, C., Danielson, L., Pando, K., Lee, C.T., 2011. Experimental determination of the metal/silicate partition coefficient of Germanium: implications for core and mantle differentiation. Earth Planet. Sci. Lett. 304 (3–4), 379–388.
Righter, K., et al., 2017. Distribution of Sb, As, Ge, and in between metal and silicate during accretion and core formation in the Earth. Geochim. Cosmochim. Acta 198, 1–16.
Righter, K., et al., 2018. Effect of silicon on activity coefficients of siderophile elements (Au, Pd, Pt, P, Ga, Cu, Zn, and Pb) in liquid Fe: Roles of core formation, late sulfide matte, and late veneer in shaping terrestrial mantle geochemistry. Geochim. Cosmochim. Acta 232, 101–123.
Righter, K., et al., 2020. Ag isotopic and chalcophile element evolution of the terrestrial and martian mantles during accretion: new constraints from Bi and Ag metal-silicate partitioning. Earth Planet. Sci. Lett. 552.
Rubie, D.C., et al., 2016. Highly siderophile elements were stripped from Earth's mantle by iron sulfide segregation. Science 353 (6304), 1141–1144.
Savage, P.S., et al., 2015. Copper isotope evidence for large-scale sulphide fractionation during Earth's differentiation. Geochem. Perspect. Lett. 53–64.
Schönbächler, M., Carlson, R., Horan, M., Mock, T., Hauri, E., 2010. Heterogeneous accretion and the moderately volatile element budget of Earth. Science 328 (5980), 884–887.
Shi, L., et al., 2022. Nitrogen isotope evidence for Earth's heterogeneous accretion of volatiles. Nat. Commun. 13 (1), 1–15.
Shirai, N., Ebihara, M., 2004. Chemical characteristics of a Martian meteorite, Yamato 980459. Antarctic Meteor. Res. 17, 55.
Siebert, J., et al., 2018. Chondritic Mn/Na ratio and limited post-nebular volatile loss of the Earth. Earth Planet. Sci. Lett. 485, 130–139.
Smythe, D.J., Wood, B.J., Kiseeva, E.S., 2017. The S content of silicate melts at sulfide saturation: new experiments and a model incorporating the effects of sulfide composition. Am. Mineral. 102 (4), 795–803.
Solomatov, V., 2015. Magma oceans and primordial mantle differentiation. Treat. Geophys. 81–104.
Steenstra, E.S., et al., 2020a. Highly reduced accretion of the Earth by large impactors? Evidence from elemental partitioning between sulfide liquids and silicate melts at highly reduced conditions. Geochim. Cosmochim. Acta 286, 248–268.
Steenstra, E.S., et al., 2020b. Metal-silicate partitioning systematics of siderophile elements at reducing conditions: a new experimental database. Icarus 335, 113391.
Steenstra, E.S., et al., 2022. Sulfur solubility in a deep magma ocean and implications for the deep sulfur cycle. Geochem. Perspect. Lett. 22, 5–9.
Suer, T.-A., Siebert, J., Remusat, L., Menguy, N., Fiquet, G., 2017. A sulfur-poor terrestrial core inferred from metal–silicate partitioning experiments. Earth Planet. Sci. Lett. 469, 84–97.
Varas-Reus, M.I., König, S., Yierpan, A., Lorand, J.-P., Schoenberg, R., 2019. Selenium isotopes as tracers of a late volatile contribution to Earth from the outer Solar System. Nat. Geosci. 12, 779–782.
Wang, Z., Becker, H., 2013. Ratios of S, Se and Te in the silicate Earth require a volatile-rich late veneer. Nature 499 (7458), 328–331.
Wang, W., Li, Y., 2024. Redox control of the partitioning of platinum and palladium into magmatic sulfide liquids. Commun. Earth Environ. 5 (1).
Wang, Z., Laurenz, V., Petitgirard, S., Becker, H., 2016. Earth's moderately volatile element composition may not be chondritic: evidence from In, Cd and Zn. Earth Planet. Sci. Lett. 435, 136–146.
Wang, H.S., Lineweaver, C.H., Ireland, T.R., 2018. The elemental abundances (with uncertainties) of the most Earth-like planet. Icarus 299, 460–474.
Wang, W., et al., 2021. Sulfur isotopic signature of Earth established by planetesimal volatile evaporation. Nat. Geosci. 14 (11), 806–811.
Wang, W., Walter, M.J., Brodholt, J.P., Huang, S., Petaev, M.I., 2023. Chalcogen isotopes reveal limited volatile contribution from late veneer to Earth. Sci. Adv. 9 (49), eadh0670.
Witt-Eickschen, G., Palme, H., O'Neill, H.S.C., Allen, C.M., 2009. The geochemistry of the volatile trace elements As, Cd, Ga, In and Sn in the Earth's mantle: New evidence from in situ analyses of mantle xenoliths. Geochim. Cosmochim. Acta 73 (6), 1755–1778.
Wood, B.J., Walter, M.J., Wade, J., 2006. Accretion of the Earth and segregation of its core. Nature 441 (7095), 825–833.
Wood, B., Nielsen, S., Rehkamper, M., Halliday, A., 2008. The effects of core formation on the Pb- and Tl- isotopic composition of the silicate Earth. Earth Planet. Sci. Lett. 269 (3–4), 326–336.
Wood, B.J., Smythe, D.J., Harrison, T., 2019. The condensation temperatures of the elements: a reappraisal. Am. Mineral. 104 (6), 844–856.
Xue, S., Li, Y., 2021. Pyrrhotite–silicate melt partitioning of rhenium and the deep rhenium cycle in subduction zone. Geology. 50, 232–237.
Yoshizaki, T., McDonough, W.F., 2021. Earth and Mars – Distinct inner solar system products. Geochemistry. 81 (2), 125746.
Young, E.D., et al., 2019. Near-equilibrium isotope fractionation during planetesimal evaporation. Icarus 323, 1–15.
Zhang, M., Li, Y., 2021. Breaking of Henry's law for sulfide liquid–basaltic melt partitioning of Pt and Pd. Nat. Commun. 12 (1), 1–9.
ZhangZhou, J., et al., 2024. Predicting sulfide precipitation in magma oceans on Earth, Mars and the Moon using machine learning. Geochim. Cosmochim. Acta 366, 237–249.